PhD Dissertations and Master's Theses

12-2020

Flexible Strain Detection Using Surface Acoustic Waves: Fabrication and Tests

Rishikesh Srinivasaraghavan Govindarajan

Follow this and additional works at: https://commons.erau.edu/edt

Part of the Aerospace Engineering Commons

FLEXIBLE STRAIN DETECTION USING SURFACE ACOUSTIC WAVES:

FABRICATION AND TESTS

By

Rishikesh Srinivasaraghavan Govindarajan

A Thesis Submitted to the Faculty of Embry-Riddle Aeronautical University

In Partial Fulfillment of the Requirements for the Degree of

Master of Science in Aerospace Engineering

December 2020

Embry-Riddle Aeronautical University

Daytona Beach, Florida

FLEXIBLE STRAIN DETECTION USING SURFACE ACOUSTIC WAVES:
FABRICATION AND TESTS

By

Rishikesh Srinivasaraghavan Govindarajan

This Thesis was prepared under the direction of the candidate's Thesis Committee Chair, Dr. Daewon Kim, Department of Aerospace Engineering, and has been approved by the members of Thesis Committee. It was submitted to the Office of the Senior Vice President for Academic Affairs and Provost, and was accepted in the partial fulfillment of the requirements for the Degree of Master of Science in Aerospace Engineering.

THESIS COMMITTEE

Daewon Kim
Digitally signed by Daewon Kim
Date: 2020.12.03 11:46:45 -05'00'

Marwan Al-Haik
Digitally signed by Marwan Al-Haik
DN: cn=Marwan Al-Haik, o=Embry-Riddle Aeronautical University, ou=Aerospace Engineering, email=alhaikm@erau.edu, c=US
Date: 2020.12.03 17:28:06 -05'00'

Chairman, Dr. Daewon Kim	Member, Dr. Marwan Al-Haik

Member, Dr. Eduardo Rojas

Graduate Program Coordinator, Dr. Marwan Al-Haik	Date

Dean of the College of Engineering, Dr. Maj Mirmirani	Date

Associate Provost of Academic Support, Dr. Christopher Grant	Date

ACKNOWLEDGEMENTS

ABSTRACT

Over the last couple of decades, smart transducers based on piezoelectric materials have been used as sensors in a wide range of structural health monitoring applications. Among them, a Surface Acoustic Wave sensor (SAW) offers an overwhelming advantage over other commercial sensing technologies due to its passive, small size, fast response time, cost-effectiveness, and wireless capabilities. Development of SAW sensors allows investigation of their potential not only for measuring less-time dependent parameters, such as pressure and temperature, but also dynamic parameters like mechanical strains. The objective of this study is to develop a passive flexible SAW sensor with optimized piezoelectric properties that can detect and measure mechanical strains occurred in aerospace structures. This research consists of two phases. First, a flexible thin SAW substrate fabrication using hot-press made of polyvinylidene fluoride (PVDF) as a polymer matrix, with lead zirconate titanate (PZT), calcium copper titanate (CCTO), and carbon nanotubes (CNTs) as micro and nanofillers' structural, thermal and electrical properties are investigated. Piezoelectric property measurements are carried out for different filler combinations to optimize the suitable materials, examining flexibility and favorable characteristics. Electromechanical properties are enhanced through a non-contact corona poling technique, resulting in effective electrical coupling. Second, the two-port interdigital transducers (IDTs) deposition made of conductive paste onto the fabricated substrate through additive manufacturing is studied. Design parameters of SAW IDTs are optimized using a second-order transmission matrix approach. An RF input signal excites IDTs and generates Rayleigh waves that propagate through the delay

line. By analyzing the changes in wave characteristics, such as frequency shift and phase

response, the developed passive strain sensor can measure mechanical strains.

TABLE OF CONTENTS

LIST OF FIGURES

LIST OF TABLES

SYMBOLS

S	=	Strain component
s	=	Elastic compliance constant
T	=	Stress component
d	=	Piezoelectric strain coefficient
E	=	Electric field component
D	=	Electric charge density component
ε	=	Relative permittivity
G	=	Voltage constant
K	=	Electromechanical coupling factor
α, β	=	Phases of PVDF
δ, γ	=	Phases of PVDF
λ	=	Acoustic wavelength
N_p	=	Number of finger pairs
L	=	Delay line distance
Wf	=	Spacing between adjacent fingers
Ew	=	Finger width
Wt	=	Acoustic aperture
BBH	=	Bus bar height
V	=	Rayleigh wave velocity
f_0	=	Center frequency
Z_0	=	Characteristic impedance
C	=	Capacitance

A	=	Area
T	=	Thickness
$F(\beta)$	=	Fraction of polar phase
A_α, A_β	=	Absorption peak intensity
k_α, k_β	=	Absorption coefficient
V	=	Voltage

ABBREVIATIONS

SAW	Surface Acoustic Wave
BAW	Bulk Acoustic Wave
MEMS	Microelectromechanical System
SH-SAW	Shear-horizontal surface acoustic wave
IDT	Inter Digital Transducer
RF	Radio Frequency
DAQ	Data Acquisition
DDM	Direct digital manufacturing
CAD	Computer aided design
DSC	Differential scanning calorimeter
DMA	Dynamic mechanical analysis
SEM	Scanning electron microscope
FTIR	Fourier Transform Infrared Spectroscopy
EDX	Energy Dispersive X-Ray
VNA	Vector Network Analyzer
COM	Coupling of Modes
IL	Insertion Loss
FDM	Fused Deposition Modeling
EBL	Electron beam lithography
ADS	Advanced Design system
DIC	Digital image correlation
PVDF	Polyvinylidene fluoride

PZT   Lead zirconate titanate

CCTO   Copper calcium titanate

CNT   Carbon nanotube

$LiNbO_3$ Lithium niobate

$LiTaO_3$ Lithium tantalite

$BaTiO_3$ Barium titanate

DMSO   Dimethyl sulfoxide

DMF   Dimethylformamide

TEP   Triethylphospate

1. Introduction

In this section, the significance, brief introduction about surface wave based sensors, piezoelectric composite material, literature review of selected SAW sensor and finally, research objective carried out in this research are discussed.

1.1. Significance

Structural health monitoring (SHM) is a class of damage detection and condition monitoring have been developed rapidly in recent days to detect damages on time, which could prevent catastrophic failure of structures with increased human safety. Commonly used SHM methods such as vibration, impedance, and guided wave based methods are used for different damage assessment in the modern community. Evaluation of aerospace structure's strain concentration due to various loads such as aerodynamic, thermal and defects necessitates a monitoring sensor system that can provide real time beneficial information. Mechanical strains for aerospace applications were commonly measured using strain gauges or piezoelectric sensors, which are commercially available sensors in the past. With the rapid development in aerospace structures, there is indeed a monitoring technique is required to guarantee the security of advanced concepts to maintain integrity, which prevents catastrophic damages.

1.2. Mechanical and Electromechanical Sensors

The mechanical sensor works based on the principle of detecting and measuring changes in response to input data causing the mechanical deformation in the intended host structure. The sensor that converts the input data into an electrical output then the sensor is named as an electromechanical sensor. The most common mechanical and

electromechanical sensors (McGrath et al., 2013) as described by the IEEE council, are

listed in Table 1.1.

Table 1.1

Major categories of commercially available sensors.

Sensor	Type
Strain gauge	- Thin and thick film - Metallic - Foil - Resistance
Acoustic wave	- Surface - Bulk
Displacement	- Capacitive - Resistive - Inductive
Pressure	- Capacitive - Piezoelectric - Inductive

   The major sensor types are piezoresistive, capacitive, piezoelectric, and photoelectric.

Among them, the most commonly used commercially available mechanical sensor is a

strain gauge, which measures the strains based on the change in resistance. The key

problem with the strain gauges and other commercially available sensors are their thermal

effects and drift errors at higher frequencies over time. An acoustic sensor, one of the

major types, is proposed to overcome these issues, which senses the measurands through

acoustic wave generation. Microelectromechanical systems (MEMS), owing to their

advantages such as micro-scale size, easy integration with the system, and less power

consumption, offer integration of sensors, actuators, and electrical devices that can measure mechanical, thermal, and chemical phenomena.

1.3. Acoustic Wave Sensor

Acoustic wave sensor is a class of microelectromechanical systems (MEMS) that is capable of sensing various parameters using wave propagation. They are classified into Surface acoustic wave (SAW) and Bulk acoustic wave (BAW) sensor (Rickert et al., 1999). The difference between both is that BAW travels through the piezoelectric substrate, but SAW travels along the piezoelectric substrate's surface. Based on the moving pattern, surface waves are classified into Rayleigh, Love, Lamb and Shear Horizontal waves (SH-SAW).

Rayleigh wave, a combination of two particle displacement components: longitudinal and transverse motion, is a two-dimensional elliptical anticlockwise particle motion wave, which propagates along the surface of an isotropic solid substrate, as shown in Figure 1.1. This wave is the simplest form of a guided wave in which amplitude decreases with an increase in depth and the reduction rate depends on the wavelength. The velocity of this wave depends on the piezoelectric material.

Lamb wave signifies a guided wave generated in plates and shell components comprising free boundaries and has two fundamental modes: symmetric and anti-symmetric. Lamb wave is similar to the Rayleigh wave, where the velocity depends on the excitation frequency and thickness of the substrate. A surface wave having a horizontal motion transverse or perpendicular to the direction in which the wave travels is a Love wave occurring with less acoustic shear velocity in the layer compared to the substrate. SH-SAW mode has particle displacement only in the normal direction to the

propagation with a unique feature that all the waves oriented perpendicular to the surface will be reflected completely, which are most attracted towards liquid phase chemical and bio applications (Nomura et al., 2006). In this research, a Rayleigh wave based SAW device is explored.
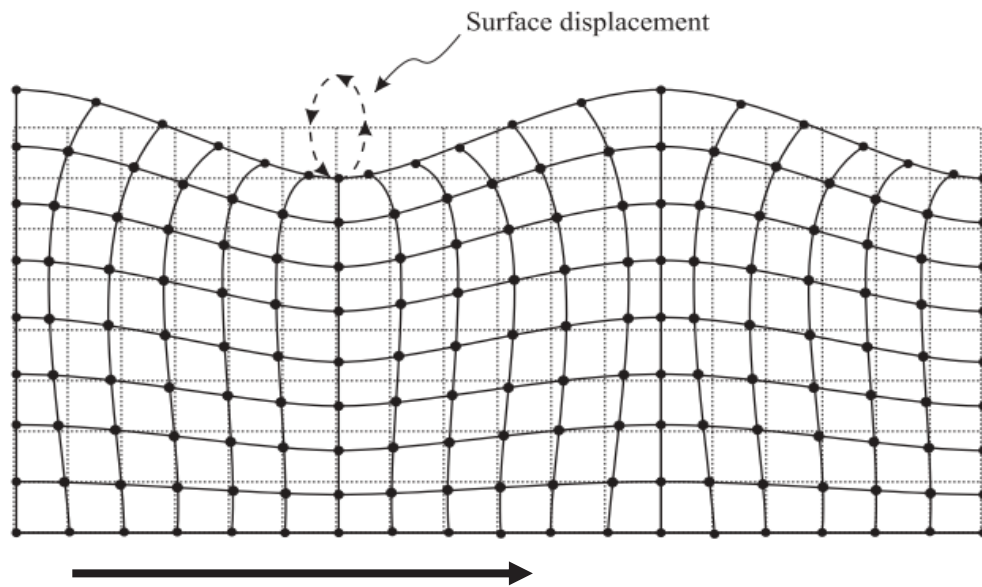
Figure 1.1 Rayleigh wave surface grid diagram (Cheeke, 2017).

As shown in Figure 1.2, the Heckmann diagram describes the coupling effect connectivity between the mechanical, electrical, and thermal properties. This diagram also gives an idea of the piezoelectric effect, especially the relation and coupling between the four components: stress T, strain S, electric field E, and displacement D (Ballato, 1995), which is utilized in sensor types utilized in this research. Detailed information about the piezoelectric effect is discussed in chapter 1.4 and other coupling presence in this diagram will be beneficial for thermal and electrical related applications.

Field E

Displacement D

Permittivity

Electromechanical effects

Electrothermal effects

Piezoelectricity

Inverse piezo effect

Direct piezo effect

Piezoelectricity

Electro caloric effect

Pyroelectricity

Pyroelectric effect

Heat of polarization

Strain S

Heat of deformation

Entropy σ

Elasticity

Piezo caloric effect

Thermal expansion

Heat capacity

Stress T

Thermal pressure

Temperature θ

Thermoelastic effects

Figure 1.2 Heckmann diagram showing coupling relation (Ballato, 1995).

1.4. Surface Acoustic Wave Sensor

In general, a device that senses a quantity such as physical or chemical changes occurred in the specific application by providing a measurable data signal containing useful information is referred to as sensors. Lord Rayleigh (1885) first discovered surface acoustic wave propagation existence and its properties. SAW devices are used to detect physical phenomena using modulation in the Rayleigh wave propagated (Prabakaran & Sujatha). This device has been widely used in engineering and commercial fields as sensors, filters, resonator, and oscillator (Aubert et al., 2009), which was started after the

IDT (Interdigital transducer) invention by R.M. White and F. W. Voltmer (1965). SAW

sensor is well known for its advantages such as passive nature, fast response time, and

cost effectiveness, as well as, its extensive applications to measure phenomena such as

pressure, temperature, strain, torque, and gas (Devkota et al., 2017; Fan et al., 2018;

Nicolay et al., 2018). SAW sensor mainly consists of the piezoelectric substrate, metallic

IDTs, and delay line where the generated wave propagates, as shown in Figure 1.3. IDTs

are used for the excitation and detection of SAW, which consists of multiple electrodes

aligned parallel and connected to the bus bars.
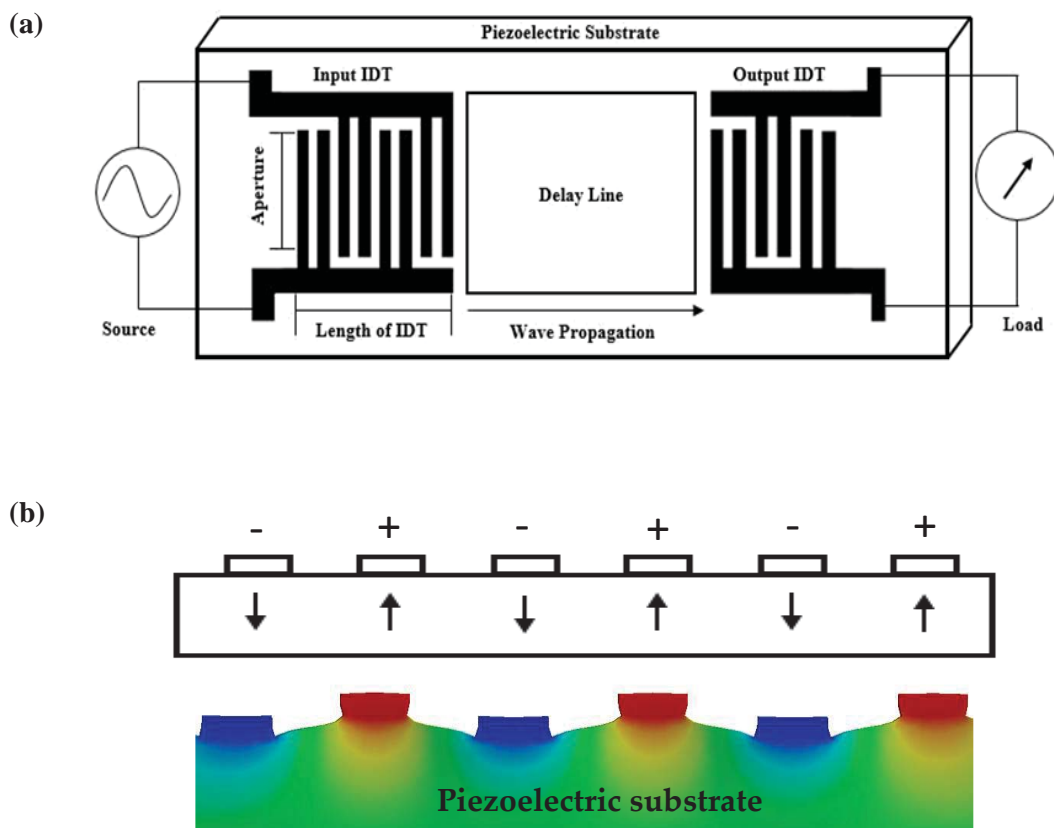
Figure 1.3 SAW sensor (a) Schematic of two-port IDTs and (b) wave generation due to voltage supply through input IDTs.

When an external force or change occurs, there will be a change in propagation path length and the density of the substrate, which changes the SAW propagation velocity. Meaning, when the strain is applied, the delay line distance between the IDTs increases, change in SAW propagation time occurs, and on the other hand, with an elliptical motion of the particles, the electric field among the particles will also be reduced. This change in SAW velocity affects the excitation of frequency. The magnitude of strain can be measured by measuring the frequency shift caused by the mechanical strains (Q. Li et al., 2019). Besides sensing the mechanical strain, SAW devices can also measure other parameters such as temperature and pressure by attaching a sensitive material in the delay line region. Commonly used sensing layers are semiconducting metal oxides and conducting/ non-conducting polymers (Ghosh et al., 2019). In the following paragraphs, the SAW sensor applications in measuring different measurands are explored.

Previously, commercially available traditional sensors such as strain gauge and thermocouple were used to measure strain and temperature occurred in aircraft engine parts (Stowell & Weise, 1983). Fiber optic grating sensor with its multi-axial capability has been utilized to measure strain in aircraft and spacecraft wings and fuselage (Udd et al., 2000). But due to their limitation such as wired setup and power supply requirements reduced the range of applications, which can be avoided by using SAW device. A two-port SAW pressure sensor made of ST-Cut quartz was fabricated, which can be operated under high temperature and pressure with 14 Hz/psi sensitivity (Della Lucia et al., 2014). Using the SAW ID tags and wired SAW Sensor principle, a passive sensor for temperature measurement with accuracy of ±0.2°C was developed within a temperature range more than 200°C distance up to 6m (Reindl et al., 1996). LGS SAW wireless

sensor suitable for higher temperature under applied strain were discussed with fewer hysteresis errors (Shu et al., 2015). SAW sensor applications based on Rayleigh wave have been developed even in the detection of a wide range of chemicals such as H_2, O_2, and CO_2. To name a few, a wireless oxygen detection SAW device made of langasite with tin oxide as a sensing layer was developed (Greve et al., 2013). A hydrogen detection method at room temperature made of $LiNbO_3$ coated with thin palladium film limited to 50 ppm was discussed (d'AMICO et al., 1982). The ability of CO_2 detection using 250 MHz ST-Quartz SAW resonator was investigated and examined a 1 kHz frequency shift with 240 ppm of CO_2 (Korsah et al., 1998).

For SAW strain measurement, the capability of SAW sensor made of $LiNbO_3$ to measure temperature and strain through radio frequency identification with a temperature and strain sensitivity of 77ppm/°C and 1 ppm/µε was demonstrated (F. Li et al., 2011). $LiNbO_3$ SAW sensor using shear horizontal wave (SH-SAW) generated through split IDT was fabricated with a 2.5 kHz/% sensitivity to monitor tire deformation (Eun et al., 2016). A single port wireless Surface acoustic wave resonator (SAWR) made of AT-X quartz to monitor strain in CNC machining tool was reported, that expands the application in condition and process monitoring applications (Stoney et al., 2012).

The longitudinal and lateral strain sensitivity measured by SAW sensor mounted on to a wafer stripe of about -0.987 ppm/µε and 0.190 ppm/µε was explored (Hempel et al., 2013). The surface transverse and Rayleigh wave modes behavior on a ST-quartz crystal was compared and addressed Rayleigh wave has better stability with positive frequency shift to perpendicular strains than STW (Fu et al., 2016). SAW sensor made of AlN film with a maximum strain sensitivity of 1.26 ppm/µε was reported (Shu et al., 2019).

Though these works provided a significant insight about strain sensing based on SAW, due to the substrate material nature, they are not suitable for high frequency range large strain applications, curved surface, and harsh environments due to their less sensitivity and drift errors over time.

1.5. Piezoelectric Effect

SAW sensor works based on the principle of piezoelectric effect. Piezoelectricity, an ability of the material to generate electric charge due to mechanical deformation. This has two effects, namely direct and inverse, which allows conversion between electrical and mechanical energy, as shown in Figure 1.4. When the piezoelectric material is subjected to mechanical deformation, the shift in positive and negative charge creates an electrical polarization resulting in electric charge generation, which is termed as the direct piezoelectric effect.

This has a secondary effect named inverse piezoelectric effect in which the mechanical wave is generated with an input electric field. Piezoelectricity comes from Greek word piezo, meaning press and this effect was discovered in 1880 by Curie brothers, who demonstrated in crystals like Quartz, Topaz, and Rochelle salt (Mould, 2007). Especially for a two port SAW device, the input IDT works under the inverse effect that generates mechanical wave in the piezoelectric substrate propagating through the delay line, and the output IDT works under the direct effect that senses the intended measurands.
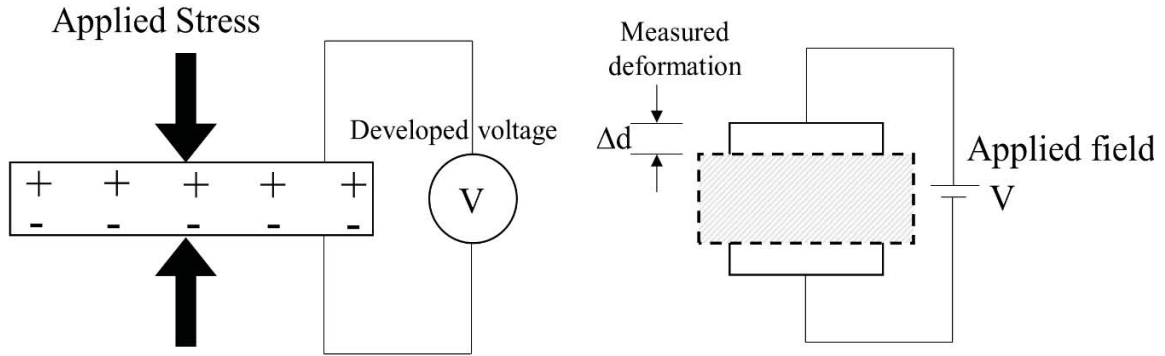
Figure 1.4 Direct and inverse piezoelectric mechanism representation.

The basic coupled constitutive piezoelectric equation describing the two piezoelectric effects for the strain or electric displacement measurement in the material is given by,

$$S = sT + d^t E \tag{1.1}$$

$$D = dT + \varepsilon E \tag{1.2}$$

where S, T, E, and D are the strain, stress, electric field, and electric charge density displacement components. The piezoelectric strain coefficient *d,* the elastic compliance *s,* and the relative permittivity ε measured at a constant electric field are associated with strain measurements (Piezoelectricity, 1987).

1.6. Crystallographic Classifications

All piezoelectric materials are non-centrosymmetric, meaning the mechanical stress can induce dielectric dipole moment. Piezoelectric, pyroelectric and ferroelectric behaviors are related to the crystalline structure of the material. From a crystallographic perspective, crystals can be classified into 32 point groups. Of these points, 21 are non-centrosymmetric with no symmetry center, and 11 are centrosymmetric non-polar crystals. Among 21 points, 20 are piezoelectric, meaning an electric dipole is generated

when a mechanical stress is applied, which exhibits polar axis with a net separation

between positive and negative charges. The remaining is one a 432 group point, which

eliminates piezoelectricity.
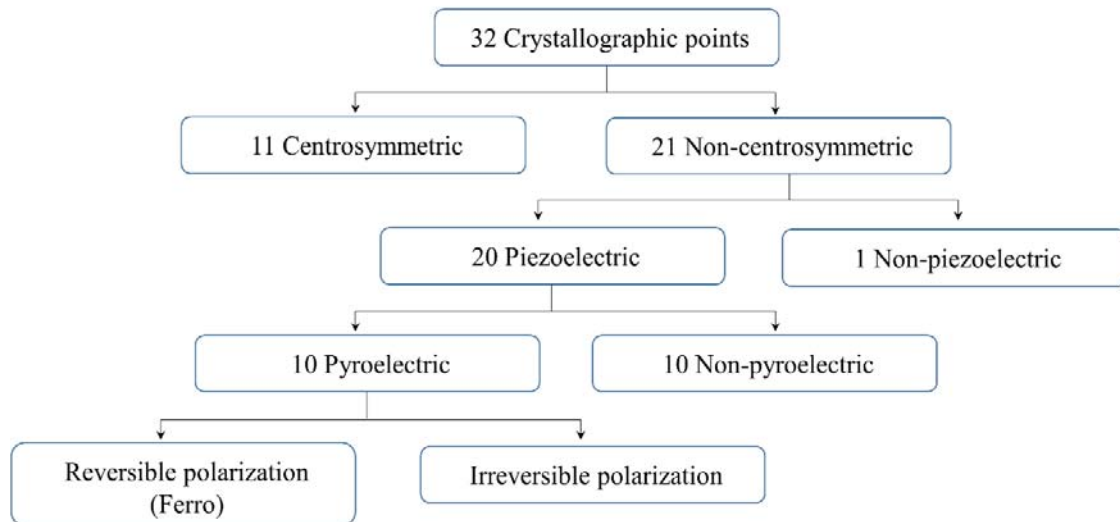
Figure 1.5 Flow chart of crystal groups (Panda, 2017).

Of the 20 piezoelectric points, 10 crystals are impulsively polarizable with variation

in the direction of dipole moment due to temperature changes. Among these 10 crystals, a

subset called ferroelectric with reversible polarization is capable of remaining polarized

even in the absence of an electric field (Defaÿ, 2013). Ferroelectric property disappears

above the materials' Curie temperature T_C. The relation between piezo-, pyro- and

ferroelectric property with crystallographic groups is shown in Figure 1.5.

1.7. Piezoelectric Composites

Piezoelectric composite, a combination of constituent phases exhibiting excellent

properties, is developing as a new material, which can be tailored on demand for specific

applications. The two phase composite geometry can be classified into 10 structures

based on each phase's connectivity (Newnham et al., 1978), which is defined as the

number of dimensions through which the material is continuous. For instance, 0-3 is

defined as 0-dimension particle embedded in 3-dimensions of continuous media. The first

digit represents the number of connectivity dimensions for the active phase (filler), while

the second digit refers to the passive phase (polymer matrix). 0-3 and 1-3 composite is

considered most useful among other types because the filler dispersed randomly in the

polymer matrix can be varied in order to increase the piezoelectric properties, as shown

in Figure 1.6. 0-3 composite is considered the simplest form in which the micro and

nanofillers weight fraction can be tailored and incorporated with the polymer matrix.

0-3 composite   1-3 composite
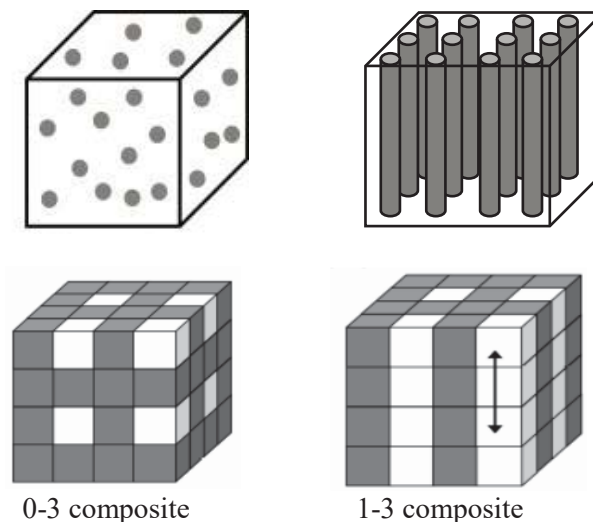
Figure 1.6 0-3 and 1-3 composite configuration (Holterman & Groen, 2013).

1.8. Piezoelectric Composite Materials

The development of composite material is a technique that eases the property

requirement by enabling the tailoring capability for intended applications. Composite is a

term representing a combination of multiphase, showing combined properties of all the

phases. For a SAW sensor, the substrate is mainly made of piezoelectric ceramics owing

to its higher piezoelectric property nature. The selection of an appropriate piezoelectric substrate material plays a vital role, which depends on its compatibility, durability, molecular structure, and electrical properties during sensor development. Major piezoelectric materials used for SAW sensor includes single crystals: lithium niobate (LiNbO$_3$), lithium tantalite (LiTaO$_3$) and ceramics such as lead zirconate titanate (PZT) (Araújo & Eiras, 1999), barium titanate (BaTiO$_3$) (Gao et al., 2007) and calcium copper titanate (CCTO) (Zhang et al., 2007).

Among these materials, commonly used fillers such as PZT, a combination of antiferroelectric lead zirconate, and ferroelectric lead titanate and CCTO are well known for their excellent dielectric constants and piezoelectric coefficients. Additionally, carbon nanotubes (CNTs) are considered as an ideal candidate as nano-fillers because of its exceptional mechanical, electrical, and thermal properties (Kumar et al., 2016). However, excessive addition of CNT fillers could reduce the breakdown strength and reaches a percolation threshold (Ferreira et al., 2013) with more than 2 wt. % influencing the piezoelectric electric field. The percolation threshold is the range of filler content in the polymer matrix, which end up showing no significant change in the piezoelectric property of the composite.

Even though these fillers exhibit higher dielectric properties they may not be suitable for flexible structures owing to their brittleness and rigid fabrication process. The crystalline lattice structure of the selected micro and nano fillers such as PZT exhibiting a perovskite structure, CCTO and SWCNTs are show in Figure 1.7. SWCNT is nothing but the rolled up version of graphene sheet.

(a)

O^{2-} Pb^{2+} Ti^{2+}, Zr^{2+}

$Pb\ [Zr_xTi_{1-x}]\ O_3$

(b)

$CaCu_3Ti_4O_{12}$

Ca

C

T

O

(c)

Graphene sheet

Rolled up
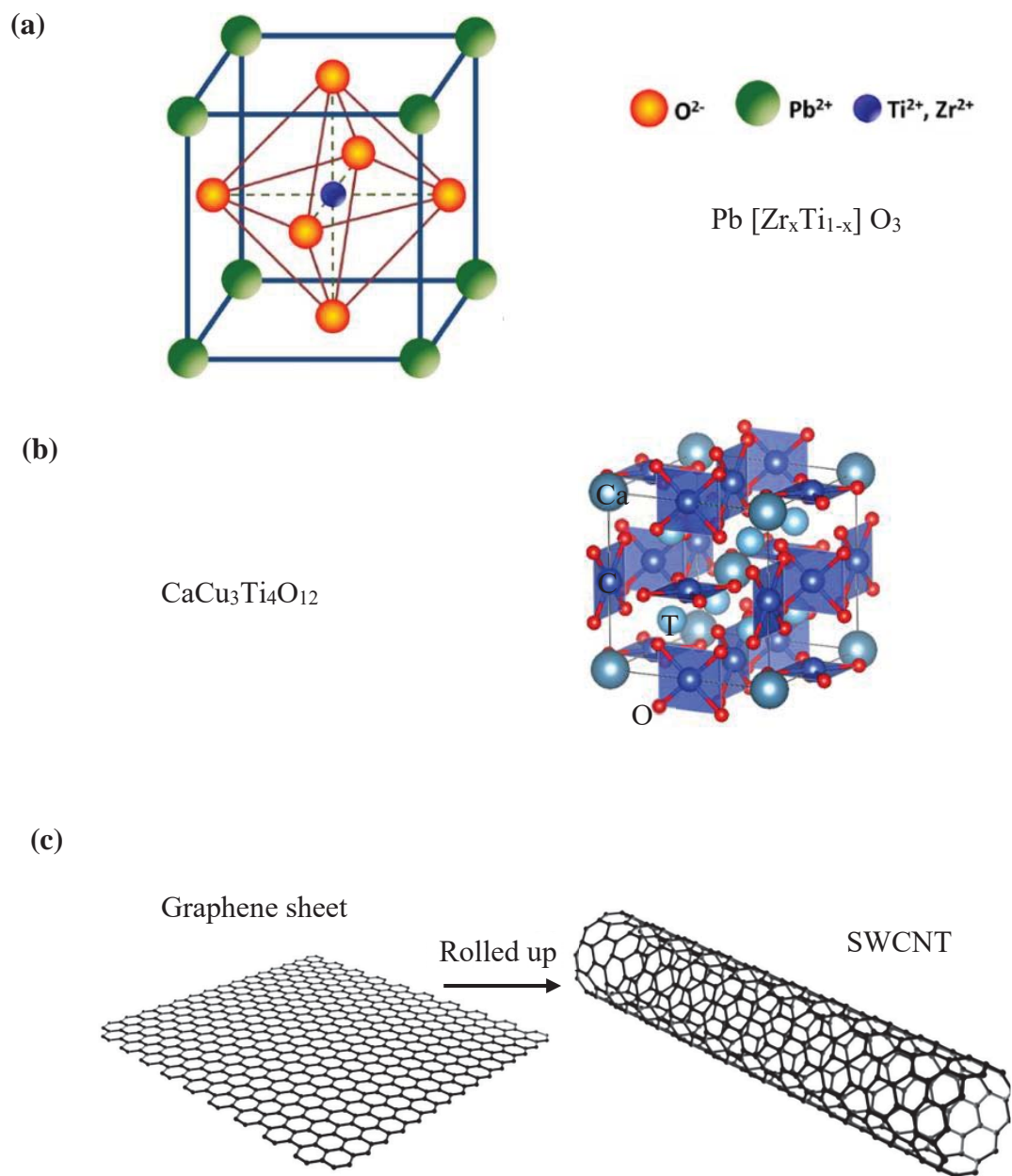
SWCNT

Figure 1.7 Lattice structure of selected micro and nano fillers (a) PZT, (b) CCTO and (c) SWCNT (Pramanik et al., 2013; Zheng et al., 2014).

On the other hand, Polyvinylidene fluoride (PVDF), an inorganic, semi-crystalline, thermoplastic fluoropolymer being flexible, exhibit excellent electromechanical coupling

with five distinct crystalline forms of different chain arrangements, as shown in Figure

1.8 (Ruan et al., 2018). However, polymer based piezoelectric materials shows less

dielectric constants and piezoelectric charge coefficients values, which limits their wave

generation efficiency. All the above mentioned challenges of polymer and ceramics

separately can be circumvented by integrating the polymer with inorganic micro- and

nano-scale fillers resulting in polymer-based composites, a new type of materials

exhibiting both flexibility and favorable piezoelectric properties that can expand the

range of applications.
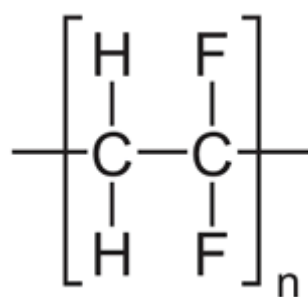
Figure 1.8 PVDF chemical structure.

1.9. Phase Information of PVDF

A semi-crystalline PVDF is a linear non centrosymmetric polymer exhibits four

major possible polymorph phases, i.e., α (trans gauche trans gauche', TGTG', nonpolar),

β (all trans, TTTT, polar), δ (TGTG', polar) and γ (T3GT3G', polar) phases where α and

β phases are most common. Among them, the essential thermodynamically stable form,

regarding the piezo-, pyro- and ferro-electric properties, is the β phase (zigzag

configuration) with all trans conformation showing higher polarity that the crystalline

region is composed of carbon backbones with fluorine arranged on one side and

hydrogen on opposite side. The β phase induces a significant dipole moment, whereas the

α phase has semi-helical antiparallel dipole conformation, which is aligned in such a way

that all dipole moment cancels each other. Materials spectrum measurements using

Fourier transform infrared spectroscopy (FTIR) and differential scanning calorimetry

(DSC) are used to study PVDF crystalline phases' contribution.

The addition of micro and nano-fillers such as CNTs and CCTO (Ouyang et al., 2015; Roy et al., 2019; Vicente et al., 2019; H. Wang et al., 2019) can increase the crystallization of PVDF, which improves the piezoelectric response of the SAW device. Different methods such as annealing, drawing, and poling are involved in the phase transition from non-polar to polar crystalline phases, as shown in Figure 1.9.
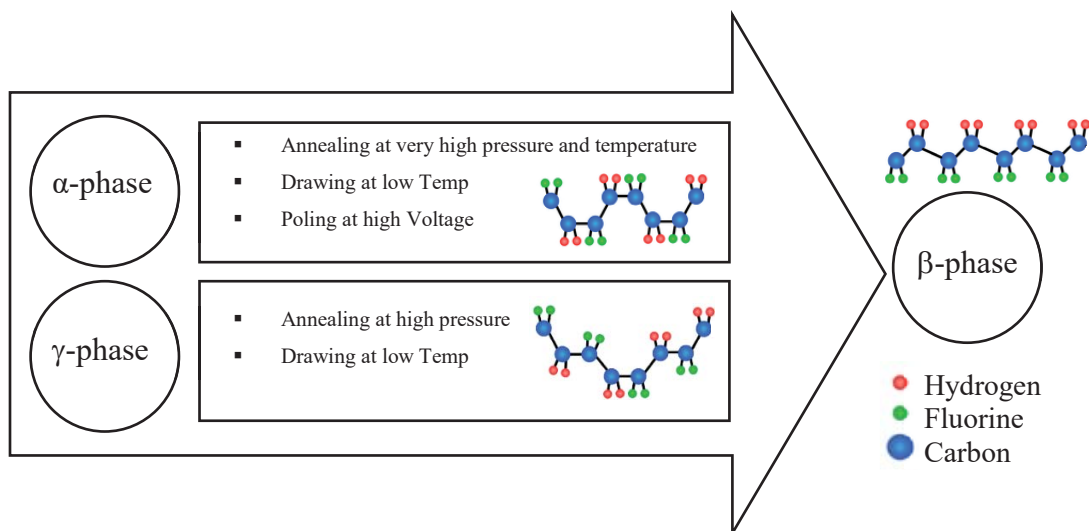
Figure 1.9 Method of transition from different conformation to obtain polar β phase (Wang et al., 2018).

1.10. SAW Sensing System

Basic principle of SAW device comprises of an RF signal received from an interrogator unit. The received input signal excites the input IDT pair initially. By utilizing the piezoelectric effects, each finger (electrode) of an IDT carries an alternative polarity ending up in electric field creation (Yao et al., 2016). IDT works under both

direct and inverse piezoelectric effect where the wave is converted back to an electrical signal with useful information for measuring the desired quantity (Mujahid & Dickert, 2017). The interrogator with the received signal is connected to the respective acquisition system to measure the required features and monitor the intended parameters. Figure 1.10 shows the overall flow of how SAW sensor works with an RF signal (Brocato, 2004).
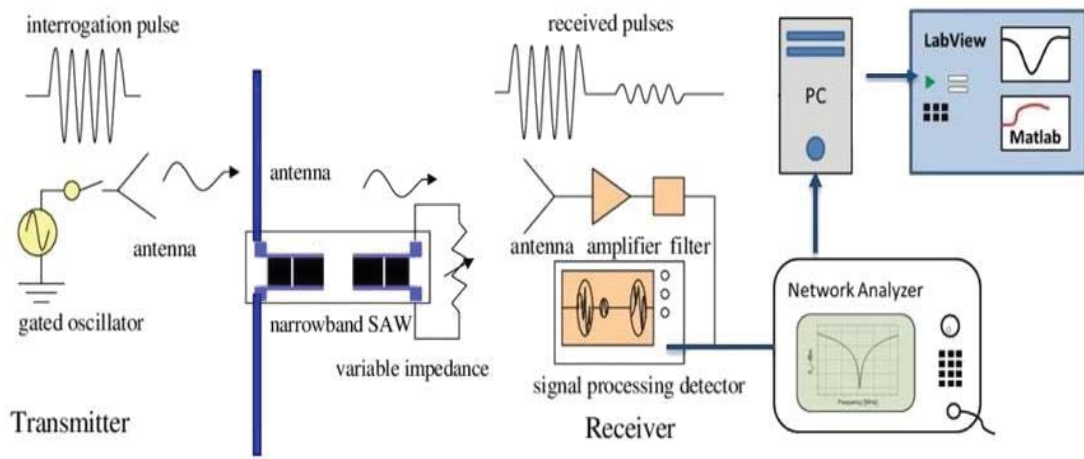
Figure 1.10 SAW sensor overall operation (Brocato, 2004).

For a SAW sensor having a wireless capability, the data collected from the output can either be stored in the server for future processing or meaningless data collected can be filtered or cleansed and processed to reduce the processing and storing capacity. Depending upon the application, the flow of the DAQ can be altered to ease the processing technique. Hardware requirements differ depending on the mode of signal transmission. For wired setup (used in this research), RF probe, fabricated SAW sensor with IDT printed on the surface, DAQ system, function generator, and VNA are required. RF probe is connected to the input and output transducers as a closed loop.

This research aims to develop a SAW sensor device in which the integral parts are piezoelectric substrate, input, output IDTs, and sensing layer or delay line region. The research starts with the piezoelectric substrate fabrication following by IDT design and optimization which is utilized to measure mechanical strains.

1.11. Research Objective

The primary motivation is to develop a new structural health monitoring system to sense and detect mechanical strains occurring in aerospace structures by using the developed SAW sensor. This thesis explores and studies the potential of piezoelectric composite-based SAW sensor and their applications in strain measurement by tracking shift in peak frequency through a novel experimental approach. Experiments include the fabrication and testing of the sensor properties with and without strains to characterize the developed strain sensor. The major research objectives are identified as follows:

a) Fabrication of piezoelectric composite substrate exhibiting flexibility through hot-press method.

b) Piezoelectric property measurement and enhancement through corona poling technique under a high electric field.

c) Deposition of designed IDT using transmission matrix approach through direct digital manufacturing.

d) Scattering parameter measurement to characterize the frequency response of the fabricated sensor attached to the host structure and correlation to the commercially used DIC.

2. Fabrication Process and Experimental Setup of SAW Sensor

In this section the two main integral parts of SAW sensor namely piezoelectric substrate with discussion about selected materials along with the fabrication process and IDT design, optimization and printing process throughout microdispensing techniques are explained.

2.1. Piezoelectric Substrate Development

The fabrication process of the piezocomposite sensor, including the solution preparation and enhancement of dipole arrangement through the corona poling technique, are discussed.

2.1.1 Materials

To fabricate a thin piezo-composite substrate, selected PVDF powder (Sigma Aldrich, USA) having an average particle size of 3-10 μm, average molecular weight Mw ~534,000 g/mol, and density of 1.74 g/ml is used to make a polymer matrix. The fillers used are PZT powder (American Elements, CA, USA, # 12626-81-2) with APS ≤ 5 μm, molecular weight Mw~ 426.29 g/mol and density of 7.5-8 g/ml, SWCNT (US research Nanomaterials, TX, USA) with an average diameter of 1.1 nm and lengths of 5-30 μm, and CCTO (Bonding chemicals, TX, USA, #535616) with a particle size of 1~5 μm, Mw ~614.18 g/mol, and density of 4.7 g/ml, due to their high dielectric constant nature and unique characteristics.

As PVDF is insoluble in water, DMSO is used to dissolve PVDF with selected fillers namely PZT, CCTO and CNTs. Figure 2.1 shows the materials purchased and used for fabrication process. All the materials are stored and utilized by following the procedures mentioned in the safety data sheets and with required PPE.

Figure 2.1 Materials used, (a) PVDF, (b) PZT, (c) SWCNTs and (d) DMSO.

2.1.2 Preparation of Piezocomposite with Hot Press Method

To fabricate a piezoelectric substrate, the polymer and ceramic are combined in the form of 0-3 composite connectivity, which is the simplest and has the capability of enhancing piezoelectric properties. PVDF, a thermoplastic fluoropolymer, has good flexibility with desirable mechanical properties. In order to circumvent the challenges to make the substrate exhibiting both flexibility and higher piezoelectric property, the selected polymer is combined with distinct micro and nano-fillers. The fillers-added polymer composites has the 0-3 pattern in which the fillers are uniformly dispersed in a three-dimensional continuous polymer matrix.

In addition, this specific configuration can be tailored as per specific requirements with ease of fabrication (Arlt & Wegener, 2010; Thongsanitgarn et al., 2010), which helps in the property and structural integrity enhancement process. These are fabricated in general through various manufacturing processes such as compression molding, extrusion, tape casting, spin coating, and hot-press. In this research, the piezoelectric substrate is fabricated using hot-press, chosen among others as it combines both the

melting and stretching techniques. The hydraulic compression press supplied by Wabash, as shown in Figure 2.2, features steel plates, a programmable controller for curing time, analog pressure, and digital temperature control.

Figure 2.2 Wabash hot-press used to cast the sample.

To fabricate the substrate, PVDF polymer with different selected ceramics and nano-fillers such as PZT, CCTO, and CNTs with respective wt. % proportions are mixed using a centrifugal planetary THINKY mixer (ARM-310), combination of both rotational and revolution axis motion maintaining homogeneity in the mixture, as shown in Figure 2.3 at 2,000 rpm for 5 minutes. As the substrate is a piezoelectric composite, the piezoelectric properties are purely based on the wt. % composition of each polymer and fillers type. In this research, different wt. % combination of PVDF and PZT has been analyzed to figure

out the optimized quantity that can meet the preferred requirements. Because too much

PZT could lead to brittle nature or excessive PVDF lack in the piezoelectric property.

Figure 2.3 ARM 310 THINKY centrifugal mixer used to mix polymer, fillers and solvent.

SEM analysis has been investigated with the purpose of selecting the best mixture of

polymer and ceramic. The proportion of other fillers such as CNTs and CCTO, are

decided based on the percolation threshold and agglomeration criteria.
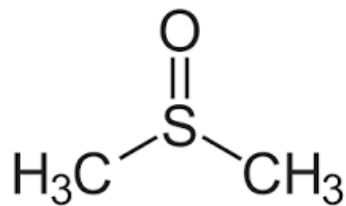
Figure 2.4 DMSO chemical structure.

The weighted powder mix is then dissolved in 30 wt. % of DMSO solvent based on the formation of a coagulated blend after mixing to get uniform dispersion. The solvent used to disperse the micro and nano-fillers and to dissolve PVDF is dimethyl sulfoxide (DMSO) (Sigma-Aldrich, USA) as PVDF is insoluble in water. Figure 2.4 shows the chemical structure of DMSO. DMSO, a polar solvent, is selected among other counterparts, such as dimethylformamide (DMF) and triethylphospate (TEP), due to its high boiling point and distinct dielectric constant (contributing to the overall electrical response), while others are hazardous in nature and a little expensive (Gonçalves et al., 2013; Gregorio Jr, 2006).

Furthermore, the coagulated mass is subjected to vacuum to eliminate air bubbles, causing a surface defect. As mentioned earlier, the hot press technique is used owing to its ease in fabrication with its capability of optimized temperature and pressure control, resulting in a denser composite with less porosity (Jain et al., 2015; Seema et al., 2007). The glutinous slurry is subjected to hot pressing at a temperature of 355° F maintained for 20 minutes curing, attaining a flat substrate that is further dried to remove the solvent.

The overall process of composite fabrication is displayed in Figure 2.5. To control and modify the sample thickness less than 1 mm, an aluminum foil is implemented while curing, instead of varying the applied pressure.

The curing temperature can be selected based on the melting temperature of PVDF, which can be defined through DSC thermogram, which is discussed in section 4.1.2. As the melting temperature of selected fillers are relatively higher than the polymer, the composite should be fine when casting with the measured melting point of the polymer matrix.
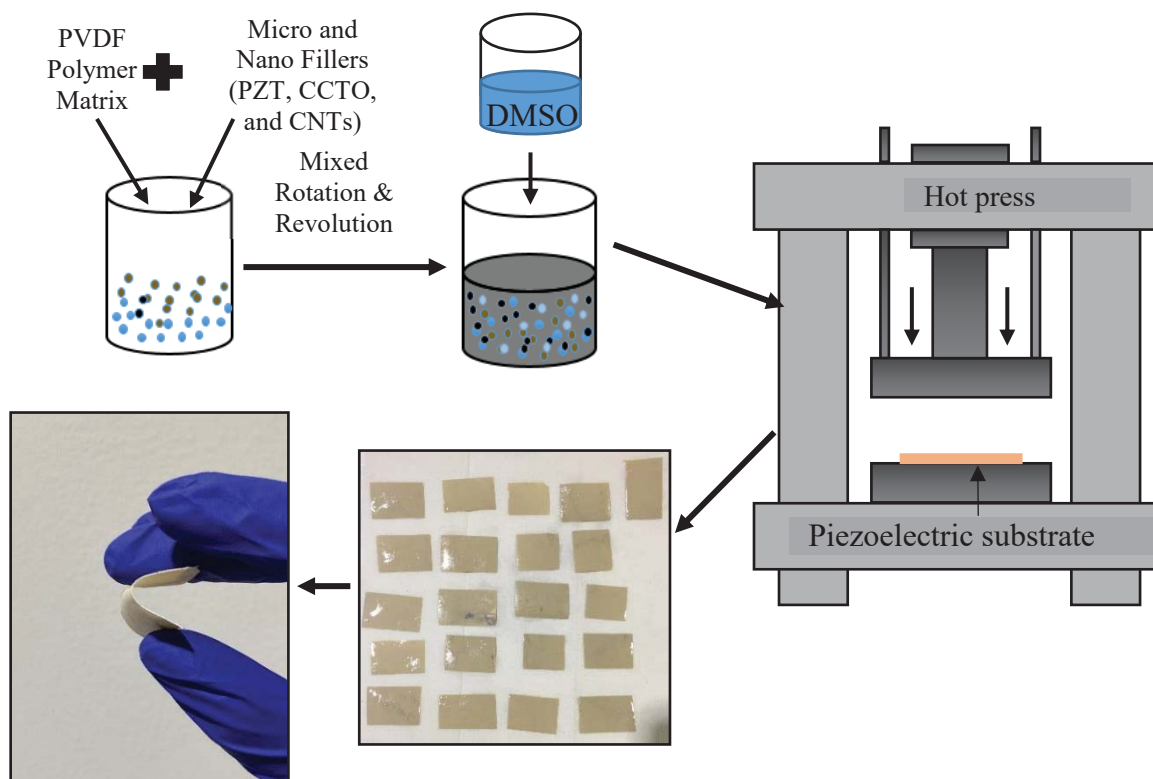
Figure 2.5 Fabrication process of Piezo-composite using hot-press technique.

Other criteria such as waviness and rigidness of the fabrication substrate are also considered to finalize the wt. % composition. As mentioned, a small amount of CNTs are included based on the percolation threshold and agglomerating nature because of strong van der Waals force leading to poor dispersion (Liu & Grunlan, 2007; Vicente et al., 2019). PVDF polymer with different filler wt. % are prepared following the same process, as indicated in Table 2.1, in which DMSO solvent proportion used are same for all the composite type fabricated. Material made through the above mentioned process are diced into favorable dimensions and all the composite type exhibits flexibility, which are then decided respective to the IDT dimensions printed in further process.

Table 2.1

PVDF polymer with different micro and nanofillers ratio used in the nanocomposite process. DMSO solvent content is same for all combinations (30 wt. %).

Sample	Thickness (mm)	PVDF (wt. %)	PZT (wt. %)	CNT (wt. %)	CCTO (wt. %)
PVDF	0.25	100	-	-	-
PVDF/PZT	0.51	40	60	-	-
PVDF/PZT/CNTs	0.82	40	59.75	0.25	-
PVDF/CNTs	0.72	98	-	2	-
PVDF/CCTO	0.60	40	-	-	60

2.1.3 Polar Phase Enhancement through Corona Poling

In order to activate the non-polar conformation to polar active β phase, it is necessary to stretch and polarize the sample under a high electric field. In our research, the stretching is already done through the hot press technique. The stretching process alone is not considered as a complete conversion of α to β phase. Electrical polarization is required to align the dipoles in the fabricated piezo-composite substrate that becomes piezoelectrically active, as shown in Figure 2.6.
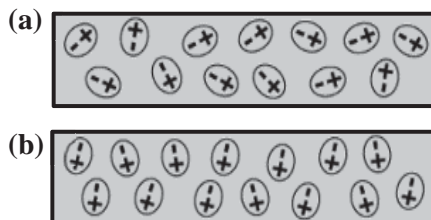
Figure 2.6 Dipole orientation before (a) and after (b) poling.

Fundamentally, there are two major poling methods, namely contact and non-contact techniques. Corona poling, a non-contact technique, presents significant advantages as it eliminates surface defect through electrode contact with the sample, where the occurrence of arcing at very high voltages is less likely, and uniform voltage distribution is attainable. In this technique, the electric charge is applied to the corona needle that acts as field intensifiers to ionize the gas molecules around the sample's top surface (unelectrode surface) to create an electric field (Kim et al., 2017; Waller & Safari, 1988).

Variables influencing the poling efficiencies are the amount of voltage supply, poling time, and distance between the corona tip as well as the sample surface (Mahadeva et al., 2013). A high voltage of 12 kV - 15 kV is applied to the sample placed 2~3 cm distance from the needle tip for 30 minutes. Piezoelectric property measurement is compared before and after poling of the different combinations selected. After the poling process, the randomly distributed dipoles are aligned along the direction of applied external electric field. Figure 2.7 shows the corona poling schematic with real setup used.
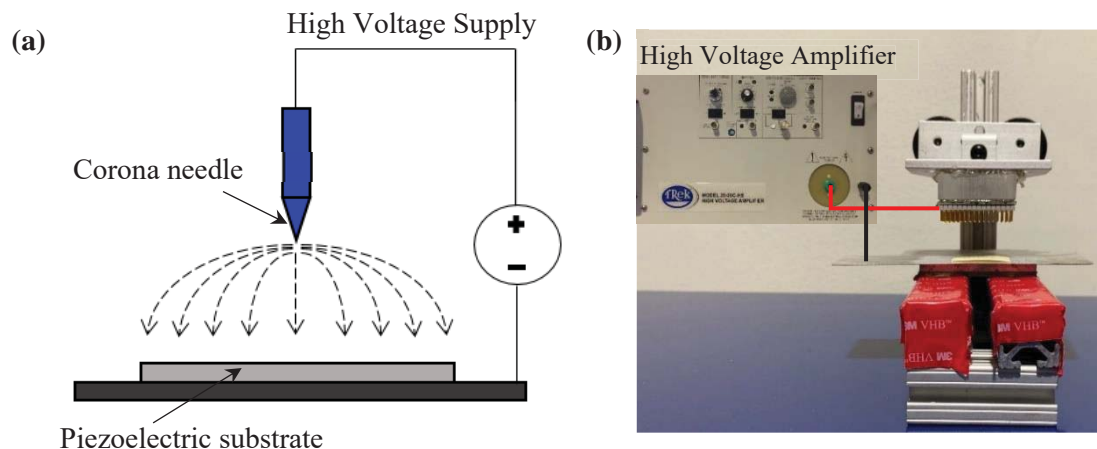
Figure 2.7 Corona poling process (a) Schematic and (b) Actual image.

2.2. Design and Modeling of Two port IDTs

In this chapter, the design and modeling of two port IDTs using a theoretical approach are discussed with attained center frequency response along with phase plot which dictates SAW sensor performance and is fabricated with the optimized dimensions through microdispensing process that utilizes the CAD model designed.

2.2.1 Transmission Matrix Approach

Depending on the method of measurement and type of parameters, various IDT designs and lines are used (Oh et al., 2012). IDT design mainly focuses on parameters like the number of finger pairs, aperture, finger spacing, finger width, and bus bar height. Commonly used IDT configurations such as a single electrode, double split electrode, and single-phase unidirectional transducers (SPUDT) are shown in Figure 2.8. The single electrode type consisting of two electrodes in each period is widely used because of its simple structure with a width of $\lambda/4$.

In contrast, a double electrode type consists of four electrodes per period with a width of $\lambda/8$ is preferred in order to precisely control the frequency response. Due to Bragg's reflection, insertion loss could be higher in a single IDT, which can be avoided using a split IDT resulting in less loss due to the different reflection frequencies (Mujahid & Dickert, 2017; A Salimi & Yousefi, 2003). In this research, single IDT is used due to the fabrication limitation, where with split IDT, the electrodes overlapped each other with less overall quality. The most commonly used SAW models to optimize and design the IDT dimensions are transmission line, coupling of modes (COM), impulse response, and superposition model.
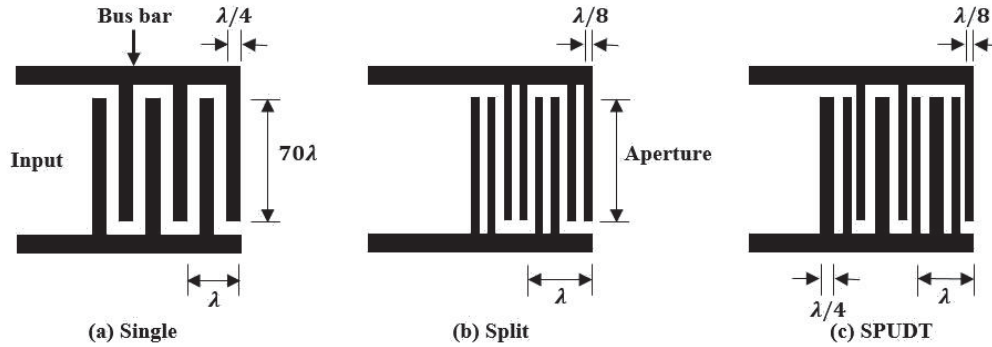
Figure 2.8 Different IDT configurations (Oh et al., 2012).

The main advantage of transmission line model, as shown in Figure 2.9, over the conventional approaches is that not only a number of second-order effects, such as reflections between fingers and transit interference, are considered but also the effect of metallization, which creates a mismatch in the acoustic impedance is taken into account. Therefore, the results obtained are expected to be relatively more accurate (Ro et al., 2004).
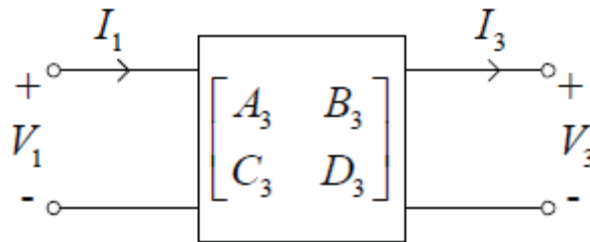
Figure 2.9 Transmission ABCD matrix.

The center frequency of the designed dimension was simulated by cascading acoustic transmission matrix respective to every SAW device element and optimized to get a favorable response with minimum insertion loss. The overall cascaded matrix is the combination of both free and metalized regions in the IDTs. Designing a two-port SAW

sensor mainly depends on the spacing between IDT and finger width, which controls the wave pattern formed. This method relates to the wave amplitudes on either side. The results of MATLAB simulation are expressed by plotting the scattering parameter in decibel (dB) and phase in degree by modifying the code from previous ERAU research work (Johannes Osse, 2017) with new IDT dimensions used, as shown in Appendix. The simulating results will vary due to input designing parameter modification. The designed SAW sensor's performance can be compared from the results obtained and further used for optimization. The SAW IDT is designed with a center frequency of 2.3 MHz and an operational frequency bandwidth of 1.5 MHz, as shown in Figure 2.10, and the IDT dimensions are shown in Table 2.2.
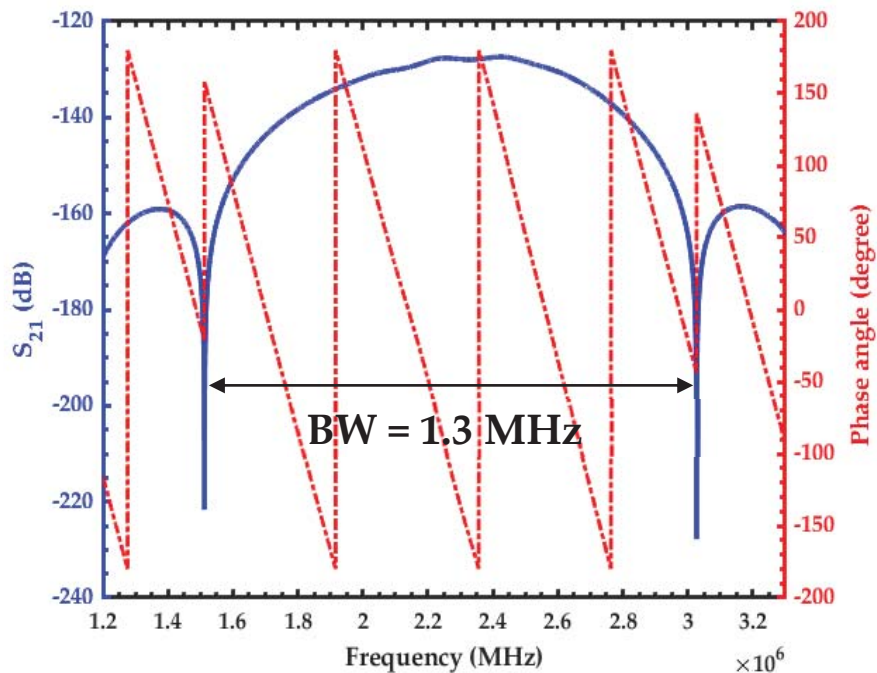
Figure 2.10 Center frequency and phase response of designed two-port IDTs.

The effectiveness of the sensor system can be identified by a various electrical feature such as insertion loss (IL), which is the loss of power that occurs as a signal travels through components or devices due to different reasons such as impedance mismatch, reflection, and power dissipated after the insertion of objects. Lower insertion loss makes detection more reliable, which reduces signal noise and increases the signal-to-noise ratio (S. Li et al., 2017). Insertion loss can be determined by frequency response analysis, measured from the transmission model and network analyzer. The phase of the output signal is influenced by any perturbation of the SAW system. A common expression of IL is shown in Equation 2.1 and is measured in decibels (dB).

$$IL = -20log_{10}|S_{21}|dB \qquad (2.1)$$

IDT with less insertion loss can be obtained by optimizing few parameters such as IDT type, IDT length, acoustic aperture, electrode type, electrode thickness, and delay line distance. The IDT metal thickness has an effect on the amplitude of the velocity shift in which thicker the metal, lower the velocity, and lesser coupling coefficient that increases the insertion loss. The ripple effect and insertion loss can be reduced by using optimal impedance matching and different IDT types to minimize reflections.

Change in delay line and finger spacing results in frequency shift. Change in length of the substrate alters the IDT finger spacing. The relation between center frequency f_0 and wavelength λ is related as $f_0 = v_p/\lambda$, determining the center frequency, where v_p is the velocity of the propagated wave that varies with different materials, the wavelength λ is the distance between two adjacent fingers of the same side, respectively.

Table 2.2

Dimensions of the fabricated SAW design.

Parameters	Dimensions
Number of input IDT pairs (Np1)	3
Number of output IDT pairs (Np2)	2
Delay line distance (L)	3.75 mm
Spacing between two adjacent IDT fingers (Wf)	0.5 mm
IDT finger width (Ew)	0.15 mm
Wavelength (λ)	1.3 mm
Acoustic aperture (Wt)	3.5 mm
Bus bar height (BBH)	0.2 mm
Wave velocity (v)	3,000 m/s
Center frequency (f_0)	2.3 MHz
Characteristic impedance (Z_0)	50 Ω

The wave velocity in the metalized section is assumed to be 3,000 m/s for this analysis (Fraga et al., 2014; Mujahid & Dickert, 2017). The shift in operational center frequency can be determined by comparing the frequency response functions (FRF) between the probed sample in flat and when it is under bending, probed in a curved surface. Nevertheless, the changes in elasticity constants such as wave velocity are also inevitable when the SAW system is subjected to the same loads. Due to differences in

both velocity and distance, the shift rate and magnitude of center frequency may be non-
linear.

2.3. Direct Digital Manufacturing of IDTs

Additive manufacturing (AM) technology has recently developed to the level where
even micro and nano scale structures, which are limited in the past to fabricate are
presently achievable for components in the field of aerospace communication and sensor
fields. It has multiple benefits, such as low cost to fabricate complex structures, freedom
of design, and automation by minimizing waste and time.

Commonly used additive manufacturing techniques are fusion deposition modeling,
superfine inkjet printing, and powder bed fusion (Kirbus et al., 2018; Ngo et al., 2018).
But due to their challenges, such as weak mechanical properties and limitations in
selecting materials, they are not well suitable for the effective printing of IDTs.
Especially, for IDT patterning, traditional techniques such as photolithography and
electron beam lithography (EBL) (Hu et al., 2019) are used. Their cleanroom necessity
and the development of complex photomask are the major limitations of traditional
lithographic techniques, which can be avoided through additive manufacturing
techniques.

In this research, a new production paradigm manufacturing technique, direct digital
manufacturing (DDM), which leads to high-quality electrode printing (Chen et al., 2015).
DDM is the process of printing the product directly from the user-defined CAD model,
which can be modified anytime by minimizing the waste in a cost-effective manner. A
DuPont CB028 conductive silver paste is used as an electrode material. The conductive
paste exhibits good adhesion to the piezoelectric substrate with higher sustainability over

the other traditional cleanroom fabrication process. A 3Dn series tabletop printer combining FDM and microdispensing capabilities with high precision motion, as shown in Figure 2.11, is used to print the designed IDT nScrypt file.
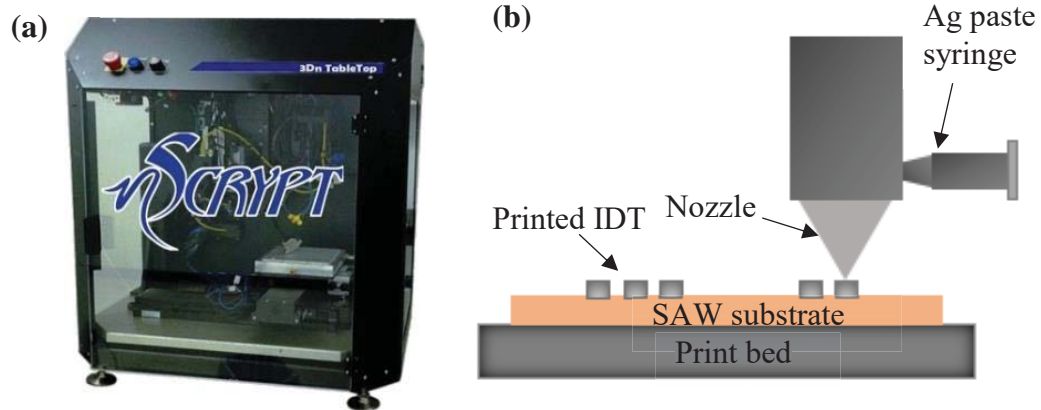
Figure 2.11 Additive manufacturing (a) 3Dn series tabletop printer and (b) Microdispensing schematic of printing conductive electrodes.

The IDT dimensions: three input pairs and two output pairs has the finger width of 0.15 mm and 0.5 mm spacing between the adjacent fingers placed 3.75 mm apart with 3.5 mm acoustic aperture, is designed using CAD and extracted nScrypt file is used to print the IDT on top of the substrate. Figure 2.12 represents the CAD model and the printed IDT with dimensions.

A nozzle of 125 μm inner diameter, 20 mm/s deposition speed, and ejection pressure of 8 psi maintained at a printing height of 100 μm from the substrate top surface. Figure 2.13 shows the SAW IDT printed on different composite types, where it can be noticed that the IDT are printed without discontinuity and coupled appropriately with the piezoelectric substrate.

(a)

(b)
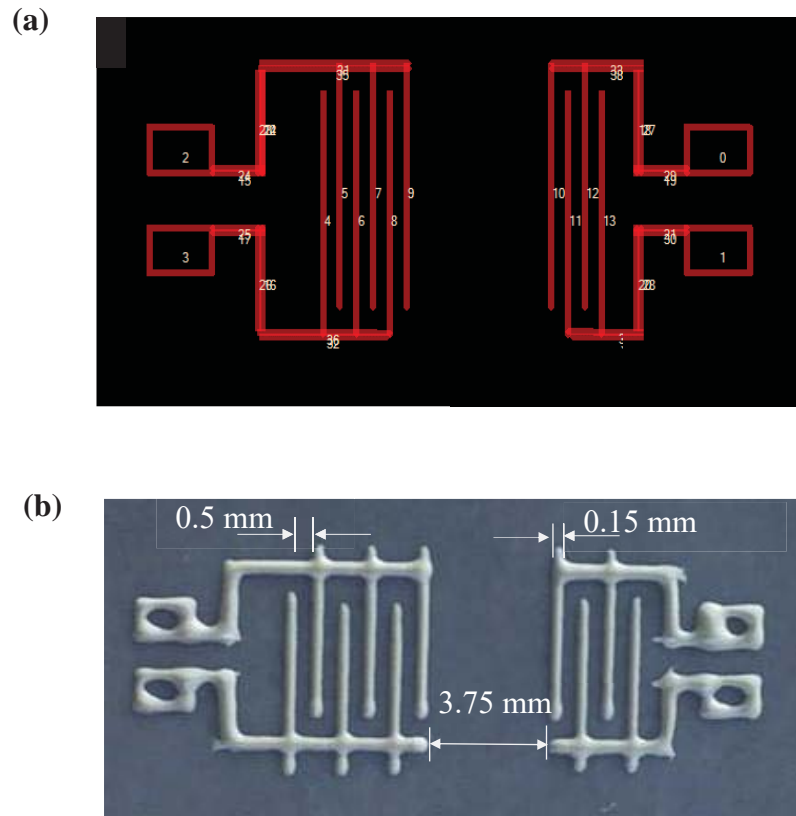
Figure 2.12 Design of IDT (a) CAD model and (b) Printed IDT with dimensions.

However, some bulb like points are still on the edge of the IDT, which can be removed with well-adjusted printing speed. Attaining a flat substrate, which reduces the time and increases the quality of IDT printing, and curing time to dry the IDT material are some of the challenges faced during the printing process. In order to increase the center frequency, the spacing of IDT can be reduced by choosing less diameter nozzle, where the overlapping of electrodes should be considered. Overall, PVDF/CCTO composite type shows better printing quality with promising structural integrity compared to other counterparts.
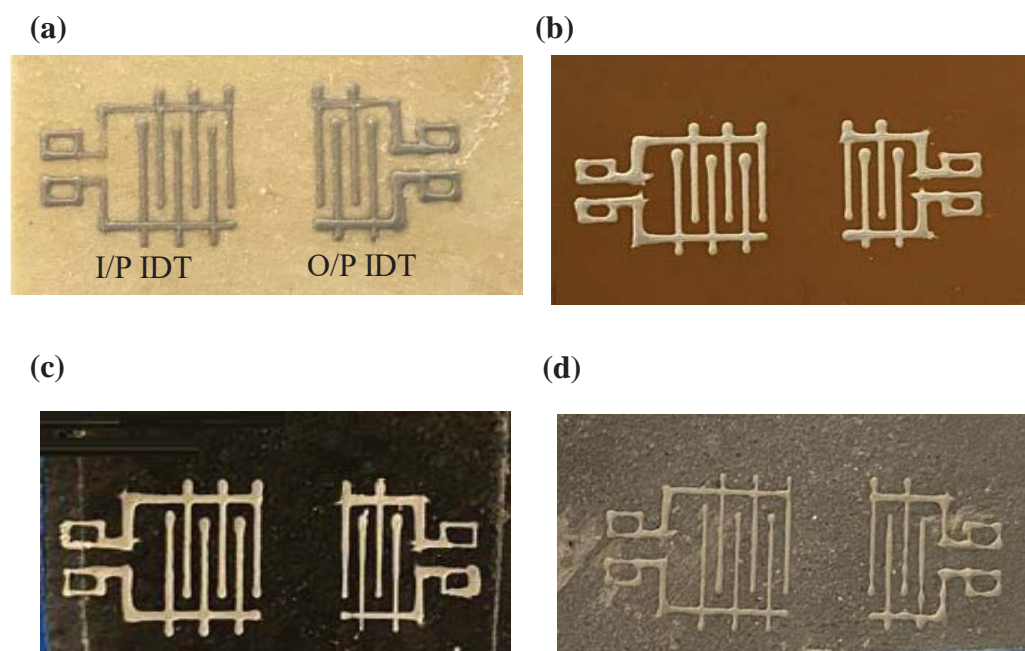
Figure 2.13 3D printed IDTs (a) PVDF/PZT, (b) PVDF/CCTO, (c) PVDF/CNTs and (d) PVDF/PZT/CNTs.

3. SAW Sensor Property Measurement

Different techniques to measure piezoelectric, thermal, viscoelastic, and morphological properties are presented in this chapter. As a quick outline, piezoelectric properties such as dielectric constant, piezoelectric strain coefficient and piezoelectric voltage constant are measured and relation in between mentioned properties are discussed. Thermal properties are measured using DSC, DMA is used to measure the storage modulus and SEM is utilized to analyze the homogeneity of different composite combinations.

3.1. Dielectric and Piezoelectric Properties

As mentioned in the constitutive Equations 1.1 and 1.2, there are some important terminologies that relates variable for certain functional applications. The piezoelectric materials can be characterized based on the significant properties such as piezoelectric stain coefficient (d_{33}), voltage (g_{33}) constant, dielectric constant (ε_r), elastic compliance (s_{33}) and electromechanical coupling factor (k).

Piezoelectric strain coefficient is the ratio of electric charge generated per unit area to applied mechanical stress or alternatively, is the mechanical strain experienced by a piezoelectric material per unit of an electric field applied, as shown in Equation 3.1.

Especially, d_{33} represents polarization induced in direction 3 per unit stress applied in direction 3, as shown in Figure 3.1 and as well as d_{31} represents polarization induced in direction 3 per unit stress applied in direction 1 (direction perpendicular to poling of piezoelectric element). It is desired to have large d_{ij} constants since it showcase the mechanical displacements, which turns out to be a huge motivation have effective transducer applications.
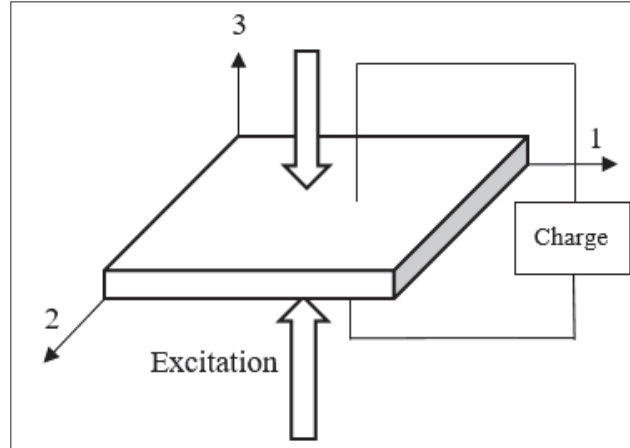
Figure 3.1 Schematic of piezoelectric strain coefficient (d_{33}).

$$d = \frac{Induced\ charge}{Applied\ Force} \qquad (3.1)$$

Dielectric constant, also called relative permittivity, is the ratio of the permittivity of the material (ε_r) to the permittivity in free space (ε_0). This constant dictates the ability of the material to be polarized under applied electric field and it purely material dependent.

In general, this dimensionless quantity can be measured in two ways namely: parallel plate capacitor theory and coplanar waveguide technique in a wide frequency range. In this work, the dielectric constant was measured using a parallel plate capacitance theory. The piezoelectric material is placed between the conductive plates to measure the capacitance, as shown in Figure 3.2. The relation to quantity dielectric constant from measured capacitance is shown in Equation 3.2.

$$\varepsilon_r = \frac{Cd}{\varepsilon_0 A} \qquad (3.2)$$

where C is the capacitance (farads), ε_0 is the dielectric constant value of free space (8.854×10^{-12} F/m), A is the area of the capacitor electrode (m^2), and d is the thickness of the piezoelectric substrate.
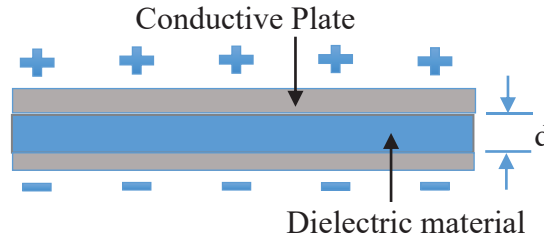
Figure 3.2 Schematic of Parallel plate capacitor.

Piezoelectric voltage constant g_{33} is the electric field generated by a piezoelectric material per stress applied or the mechanical strain experienced per unit displacement applied. Particularly, g_{33} denotes electric field induced in direction 3 per unit stress applied in direction 3. This property can be calculated by using the ratio between measured piezoelectric strain coefficient and dielectric constant, as shown in Equation 3.3.

$$g_{33} = \frac{d_{33}}{\varepsilon_0 \varepsilon_r} \tag{3.3}$$

Electromechanical coupling coefficient is an important factor in validating energy conversion efficiency from electrical to mechanical or vice versa. It can be calculated using other parameters mentioned as, where s_{ij} is the elastic compliance of the piezoelectric material, as shown in Equation 3.4.

$$k_{ij} = \frac{d_{ij}}{\sqrt{\varepsilon_{ij} s_{ij}}} \tag{3.4}$$

3.2. Thermal Analysis using DSC

Differential Scanning Calorimeter (DSC) is a thermal analytical technique used to study the enthalpy changes and thermal transitions in the polymer and ceramic mix due to the change in their chemical properties as a function of temperature or time. DSC 3 Mettler Toledo, with an operating temperature range of -150 °C to 700 °C, as shown in Figure 3.3, is used in which the heat transfer rate and energy required to maintain zero difference between the sample and reference are analyzed.
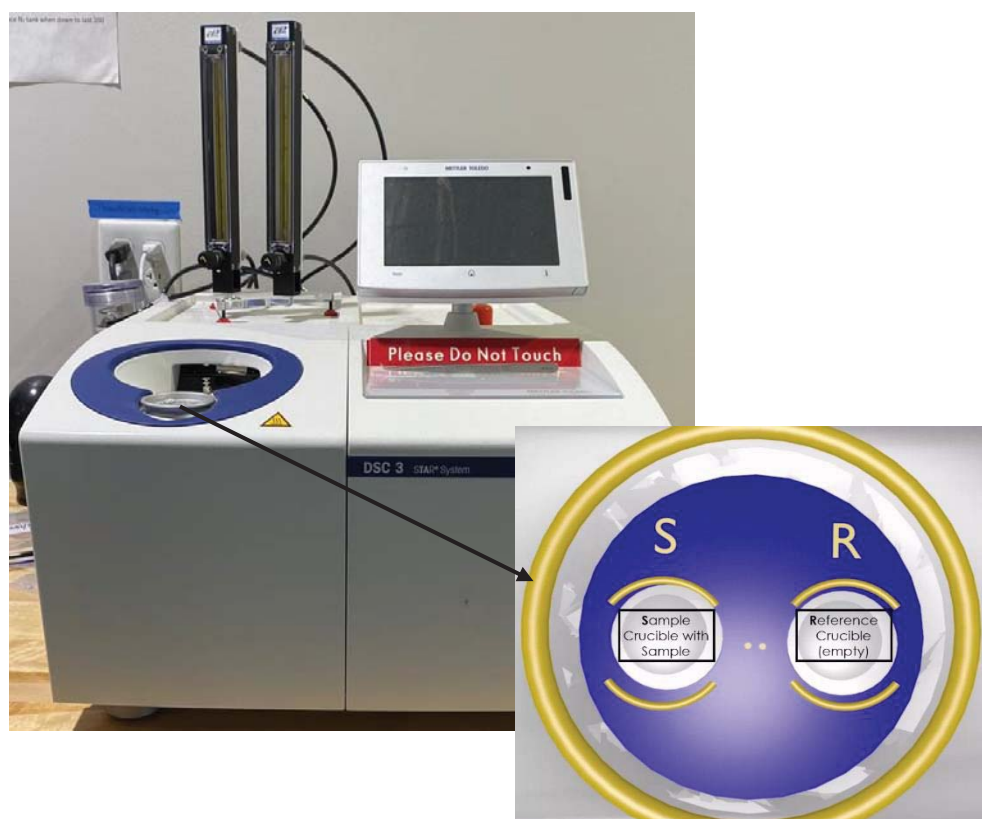
Figure 3.3 DSC calorimeter with zoomed in figure showing sample and reference crucible.

In general, properties such as melting point, glass transition temperature, degree of cure are measured. Melting temperature (T_m), a major thermal transition is analyzed where the arrangements inside the polymer chain begin to move freely with an extra heat flow showing an endothermic peak. In order to get a thermogram, the first step is to switch on the DSC with the chiller and adjust the flow rate of nitrogen to 10 mL/min. To measure only the coagulated mass of PVDF with solvent, an aluminum crucible is zeroed using a balance, and PVDF was encapsulated using the punching machine. The sample was then placed in the sample holder next to the reference crucible to go through the isothermal and dynamic test.

3.3. Viscoelastic Analysis using DMA

The Dynamic mechanical analysis (DMA) is a technique used to characterize materials especially viscoelastic behavior of polymers and ceramics. DMA 8000 PerkinElmer apparatus is used to characterize the material stiffness for the different composite configuration with a temperature sweep at constant pressure. A sinusoidal deformation is applied to the sample with a known geometry where the sine wave is transmitted to the sample through drive shaft.

In general DMA has multiple fixtures such as compression, three point bending, tensile and single cantilever respective to the structure of the sample and by knowing the fabricated composite samples are thin and flexible, tensile fixture is used. As shown in Figure 3.4, the sample with known dimensions are clamped in the fixture and mechanical analysis were carried out with respective temperature sweep.
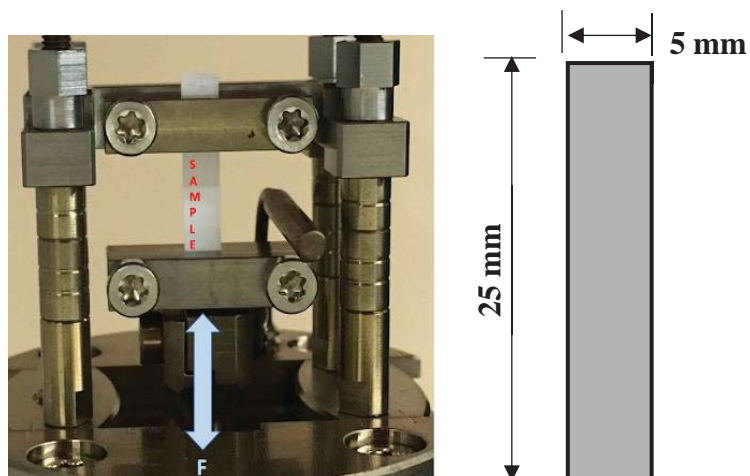
Figure 3.4 DMA tensile fixture with sample dimensions.

3.4. Morphological analysis using SEM

Scanning electron microscope (SEM) technique examines the surface of the piezo-composite substrate in order to observe and analyze the particle distribution, morphological homogeneity and dispersion of the polymer with selected fillers after hot-pressing. The fabricated composite is analyzed using a FEI Quanta 650 SEM machine, as shown in Figure 3.5. All samples were coated with ~ 0.2 µm Gold for better conduction while imaging. Particle size were determined quantitatively by taking an average of the size viewed in the scanned microscope image.

Figure 3.5 SEM microscope.

4. Results and Discussions

Using the previously defined experimental techniques, various results including crystalline phase, morphological, piezoelectric, dielectric, mechanical properties, and strain measurements through RF testing of the fabricated composites, and strain quantification and correlation with DIC are presented and discussed in this section. In order to validate the efficiency of the selected substrate material, knowing the above mentioned properties will be beneficial.

4.1. Material Spectral Analysis

PVDF polymer are semi crystalline in nature in which its behavior with selected fillers needs to be validated through spectral analysis such as FTIR, Raman and EDX. These information will gives a supporting information of how the crystalline phase and functional group presence contributes to the piezoelectric properties are discussed.

4.1.1. Chemical Characterization using FTIR

FTIR is a technique used to obtain an infrared spectrum of absorption and crystalline structure elucidation to identify the functional group of the molecules of a material with phase information. An IR spectrum is passed through the sample in which some of the radiation is absorbed by the bonds between different elements at different frequencies resulting in a spectrum representing the molecular structures. By identifying the spectrum against a database of reference spectra, materials can be determined especially when a polymer is incorporated with micro and nanofillers. As PVDF polymer exhibits distinct crystalline phases, it is important to analyze the crystalline structure, supporting to distinguish between the different phases with their unique characteristics. The sample

should be thin enough for the IR to pass through, and as the fabricated composite was thin, it was well suited for the desired technique.

Figure 4.1 Agilent FTIR spectrometer.

FTIR allows to identify the molecular structure and dynamics of a polymer in which the peak phases are classified into three major categories, i.e., 1) common peaks that appear in all crystalline phases; 2) peaks exclusive for one of the phases; 3) dual peak combining different phases. As fillers are added to the base polymer in this research, in order to analyze the effect of different fillers, FTIR spectra are compared for the different composite types. An Agilent Cary 630 FTIR spectrometer with a diamond crystal, as shown in Figure 4.1, is operated in the wavenumber of 650-1550 cm^{-1} measured with a resolution of 4 cm^{-1} and 16 scans followed with automatic background correction.

From the collected FTIR spectra, as shown in Figure 4.2, the corresponding bands confirm the presence of α phase in the sample at 762 cm^{-1} (CF$_2$ bending and rocking, 873 cm^{-1} (C-F stretching), and 1069 cm^{-1} (C-C-C bonding). In contrast, the characteristics bands of β phase are at 835 cm^{-1} (trans chain sequence CF$_2$ stretching and CH$_2$ rocking),

1168 cm^{-1} (C-C bonding), 1230 cm^{-1} (F-C-F bonding), 1401 cm^{-1} (CH$_2$ wagging

vibration) and 1427 cm^{-1} (CH$_2$ bending), as listed in Table 4.1. The experimental spectra

show indeed a close resemblance of majority peaks and a slight variation in some specific

peaks due to the fact that PVDF is formed utilizing a different technique (Benz & Euler,

2003; Cai et al., 2017; Medeiros et al., 2018; Peng et al., 2008; P. Wang et al., 2019).

Additionally, a peak around 3400 cm^{-1} arises due to O-H bond of carboxylic acid in the

solvent. Change in intensity of the spectra signifies changes corresponding to the sample

composition related to the bonds or phase or crystallinity with the respective fillers.

Change in the dipole moment of the bond and the number of specific bonds present

predicts the absorption intensity. The bond dipole depends on major factors such as the

bond length and charge difference between the atoms.

Table 4.1

Wavenumber assignment of FTIR analysis.

Wavenumber	Crystalline phase	References
762 cm^{-1}	α phase	CF$_2$ bending and rocking
835 cm^{-1}	β phase	Trans chain sequence CF$_2$ stretching/ CH$_2$ rocking
873 cm^{-1}	α phase	C-F stretching
1069 cm^{-1}	α phase	C-C-C bonding
1168 cm^{-1}	β phase	C-C bonding
1230 cm^{-1}	β phase	F-C-F bonding
1401 cm^{-1}	β phase	CH$_2$ wagging vibration
1427 cm^{-1}	β phase	CH$_2$ bending

In order to determine the fraction of β (active-polar) phase in each type of filler added to PVDF polymer, IR absorption corresponding to bands at 762 cm^{-1} and 835 cm^{-1} is taken into account. Based on Beer-Lambert law (Ali Salimi & Yousefi, 2004; Sanati et al., 2018), the relative fraction of the β phase is quantified as mentioned in Equation 4.1, where A_α and A_β are the absorbance peak intensities at the 762 cm^{-1} (α phase) and 835 cm^{-1} (β phase); k_α and k_β are the absorption coefficient, which values are 7.7 x 10^4 cm^2 mol^{-1} and 6.1 x 10^4 cm^2 mol^{-1}, respectively. Using the Equation 4.1, the polar phase fraction for the different composite types is shown in Figure 4.3. It is evident that adding fillers to the PVDF polymer contributes in active β phase enhancement and PVDF/CNTs composite yields the maximum β phase fraction of 76.9% while comparing with the counterparts.

$$F_\beta = \frac{A_\beta}{\left(\frac{k_\alpha}{k_\beta}\right) A_\alpha + A_\beta} \tag{4.1}$$
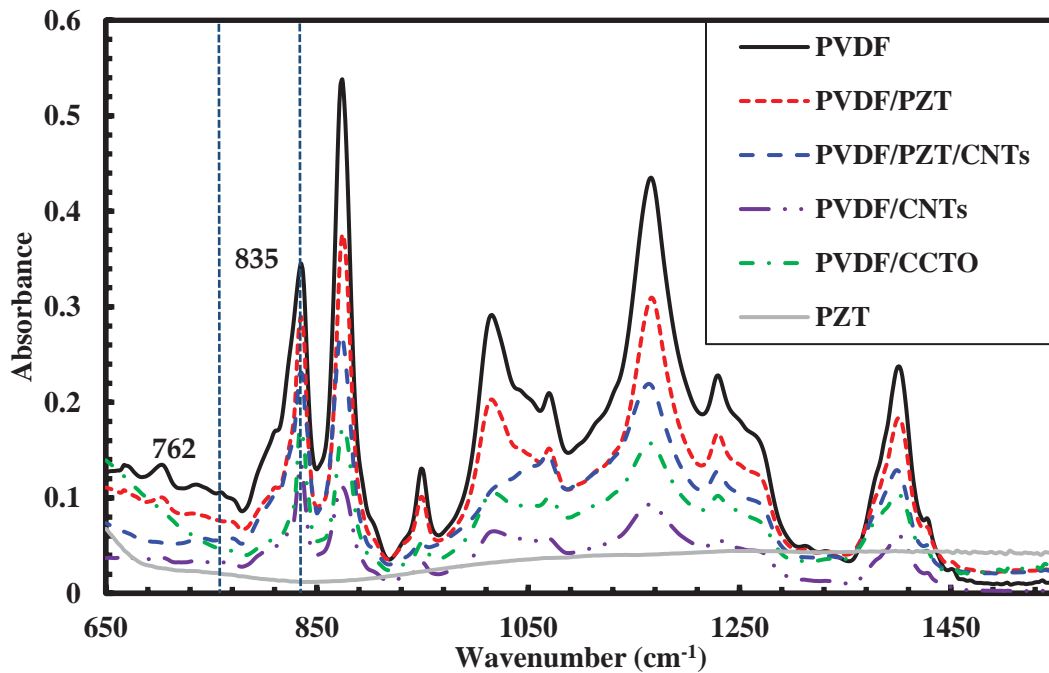
Figure 4.2 FTIR absorbance spectra of different fillers with PVDF polymer.

This quantification helped to scientifically prove that through the hot press (stretching) and applying a high electric field with corresponding fillers, the other crystalline phases can be converted into a polar phase. But in order to characterize the presence of specific functional groups in CNTs and CCTO, additional technique such as Raman spectroscopy is recommended.
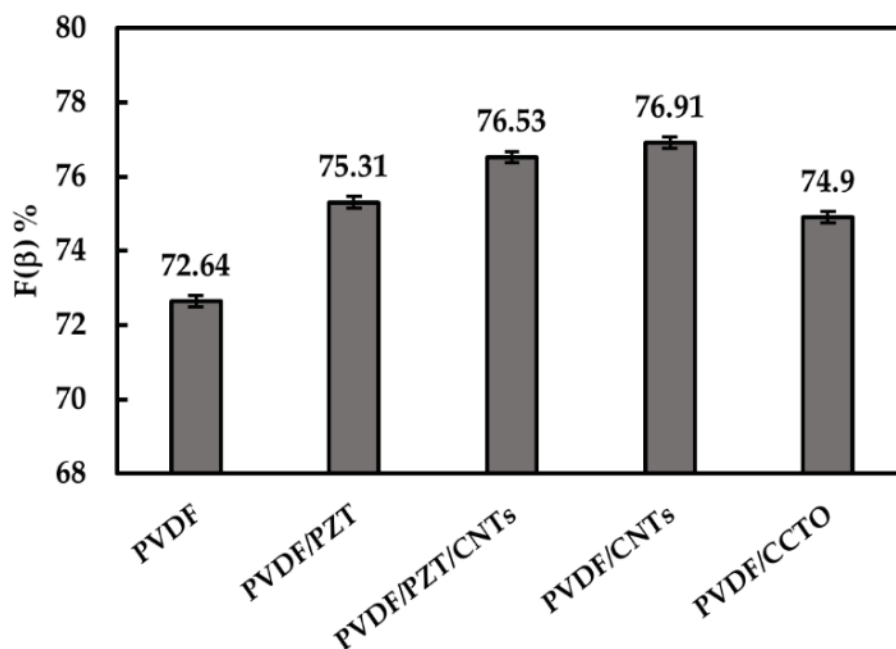
Figure 4.3 Relative fraction of calculated polar β phase.

4.1.2. Thermal Characterization

To evaluate the thermal properties of PVDF polymer, DSC is carried out using a Mettler Toledo calorimeter in the temperature range from 0 °C to 180 °C at a heating rate of 1°C/min. Figure 4.4 thermogram shows PVDF is strongly influenced by the temperature during the melting process from 145 °C to 170 °C. It is noticed that double endothermic fusion peak occurred with 5 °C difference at 156 °C and 161 °C due to the

melt recrystallization whereas the peak belongs to α and β phases (García-Zaldívar et al., 2017; Peng et al., 2008).
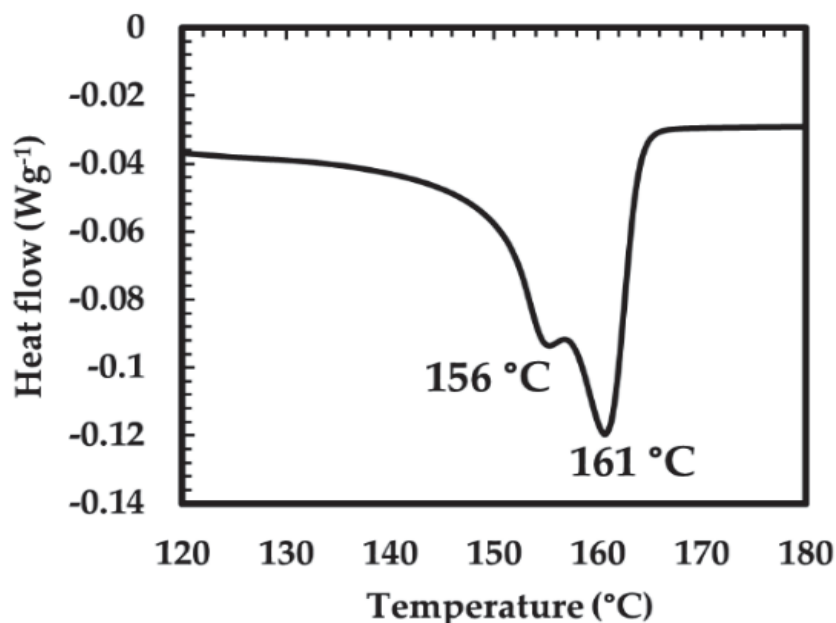
Figure 4.4 DSC curve of PVDF sample showing endothermic peaks.

4.1.3. Raman Shift Analysis

Raman analysis is preferred to detect the presence of CNTs as they are a black body that absorbs all lights and ending up with a lot of noises in the spectra. The main noticeable bands for CNTs through Raman analysis are the high frequency D (disordered), G (graphite), and radial breathing modes (RBM) modes. G mode is a tangential shear mode of carbon atoms, D band is a defect mode requires while elastic scattering to conserve momentum and RBM is associated with the symmetrical movement of carbon atoms.
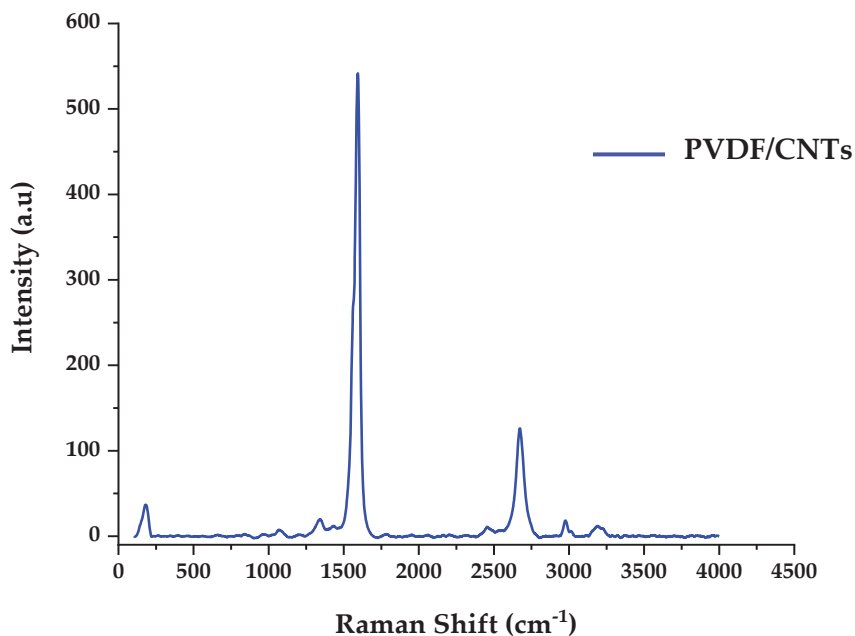
Figure 4.5 Raman spectra of PVDF/CNTs.

From the Figure 4.5 and 4.6, the peak below 300 cm^{-1} is due to the symmetric radial vibrations of carbon atoms, D-line ranges between 1300 and 1400 cm^{-1} in which the peak at 1343 cm^{-1} is due to the surface and structural defects, the G-band ranges from 1500 to 1700 cm^{-1} in which peak at 1594 cm^{-1} is due to the longitudinal and transversal in-plane phonon, and 2D-band peak at 2658 cm^{-1}, which is the symmetry overtone of D band (Kharlamova et al., 2018; Yan et al., 2013). Raman spectra with a laser wavelength of 532 nm excitation is used to examine all the four main regions in CNTs. From the D/G ratio, purity and defects in SWCNTs can be quantified (Miyata et al., 2011; Tsentalovich et al., 2017). Even though knowing the defect percent information will be beneficial, the main idea of Raman analysis is to characterize the presence of SWCNTs incorporated with PVDF and PZT, respective composite types.
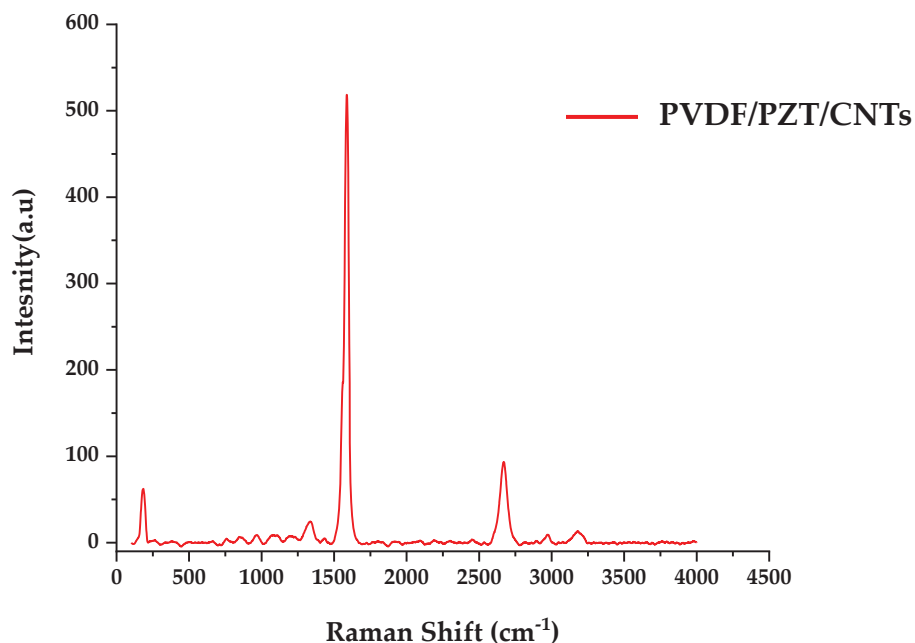
Figure 4.6 Raman spectra of PVDF/PZT/CNTs.

The three main modes A_g (1) at 448 cm^{-1}, A_g (2) 510 cm$^{-1,}$ and F_g (3) at 576 cm^{-1} appeared in the plots confirms the presence of CCTO, as shown in Figure 4.7. The scattering modes appeared A_g (1), and A_g (2) are associated with TiO_6 rotation like vibrations. F_g (3) mode is associated with antistretching vibrations of O-Ti-O (Kang et al., 2014; Kawrani et al., 2019; Thiruramanathan et al., 2018). From all the above discussed and measured peaks through Raman shift analysis, the presence of CNTs and CCTO fillers are ensured which was limited through FTIR analysis. The majority of the peaks show resemblance with references and slight variation in specific peaks because of the products purchased from different manufacturers and different technique utilization.
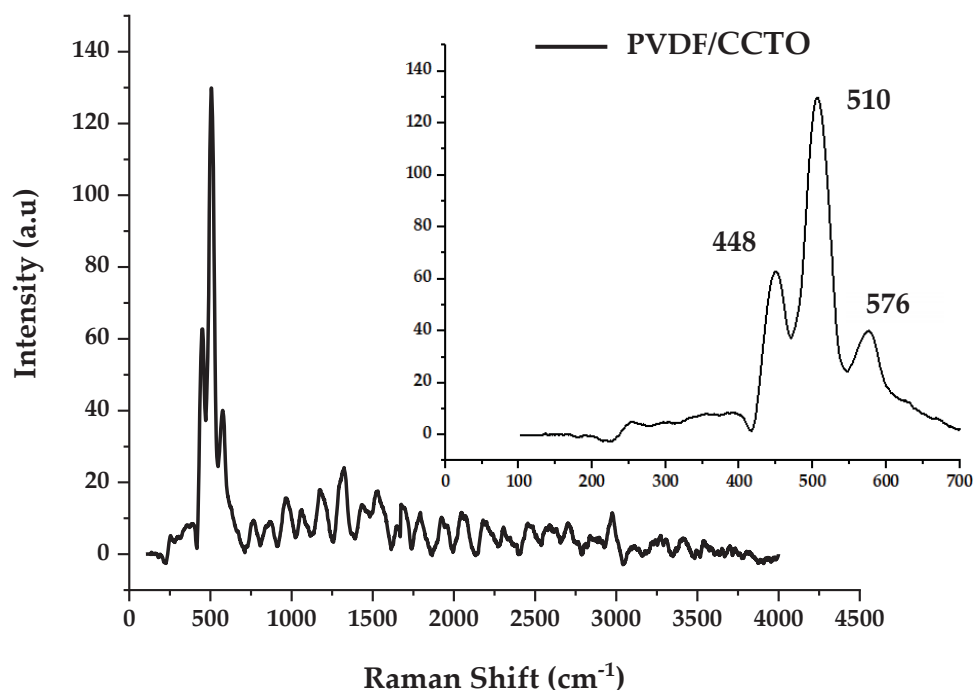
Figure 4.7 Raman spectra of PVDF/CCTO; zoomed in figure shows the major peaks of CCTO.

4.1.4. EDX Analysis

The chemical composition of PVDF/CCTO composite type was measured using an energy dispersive X-Ray spectroscopy (EDX, Bruker). Every single elements in PVDF/CCTO composite were evaluated to examine the presence of C, F, Ca, Cu, Ti, and O based on stoichiometry, as shown in Figure 4.8. As the samples are coated with gold to be more conductive, Au presence is also detected along with confirmed other elements presence. Since H 1s are valance electrons, which has extremely small photoelectron cross-section and cannot share its only electron in forming compounds, it is difficult to detect hydrogen atoms.
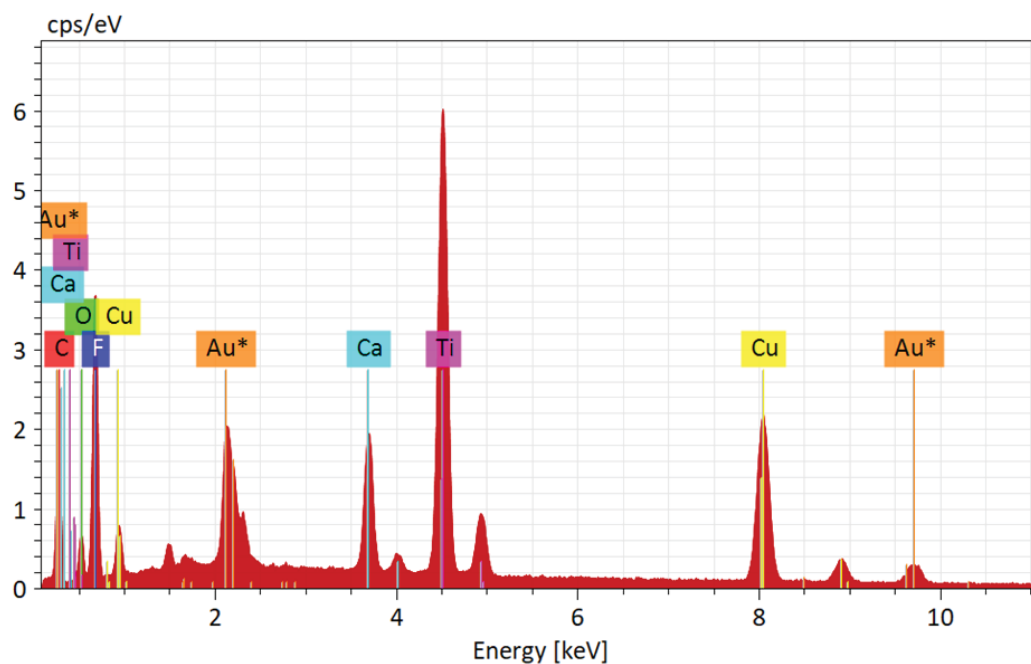
Figure 4.8 EDX spectra of PVDF/CCTO composite.

4.2. SEM Analysis

By using Quanta 650 SEM machine, different wt. % of PVDF/PZT are analyzed, as shown in Figure 4.9, where the microparticles are well dispersed in the 40-60 wt. % combination with less agglomeration, well-adhered with no pores, uniform distribution, and PVDF particle with an average particle size of 3~7 μm is observed. 80-20 wt. % and 60-40 wt. % combinations exhibit flexibility with less stiffness, high agglomeration with reunion phenomenon, shrinking nature, and waviness not suitable for transducer deposition. Composite with less polymer matrix is fragile because of ceramic's brittle nature. It is noticed that when the PVDF content increases, the agglomeration develops, affecting structural integrity.
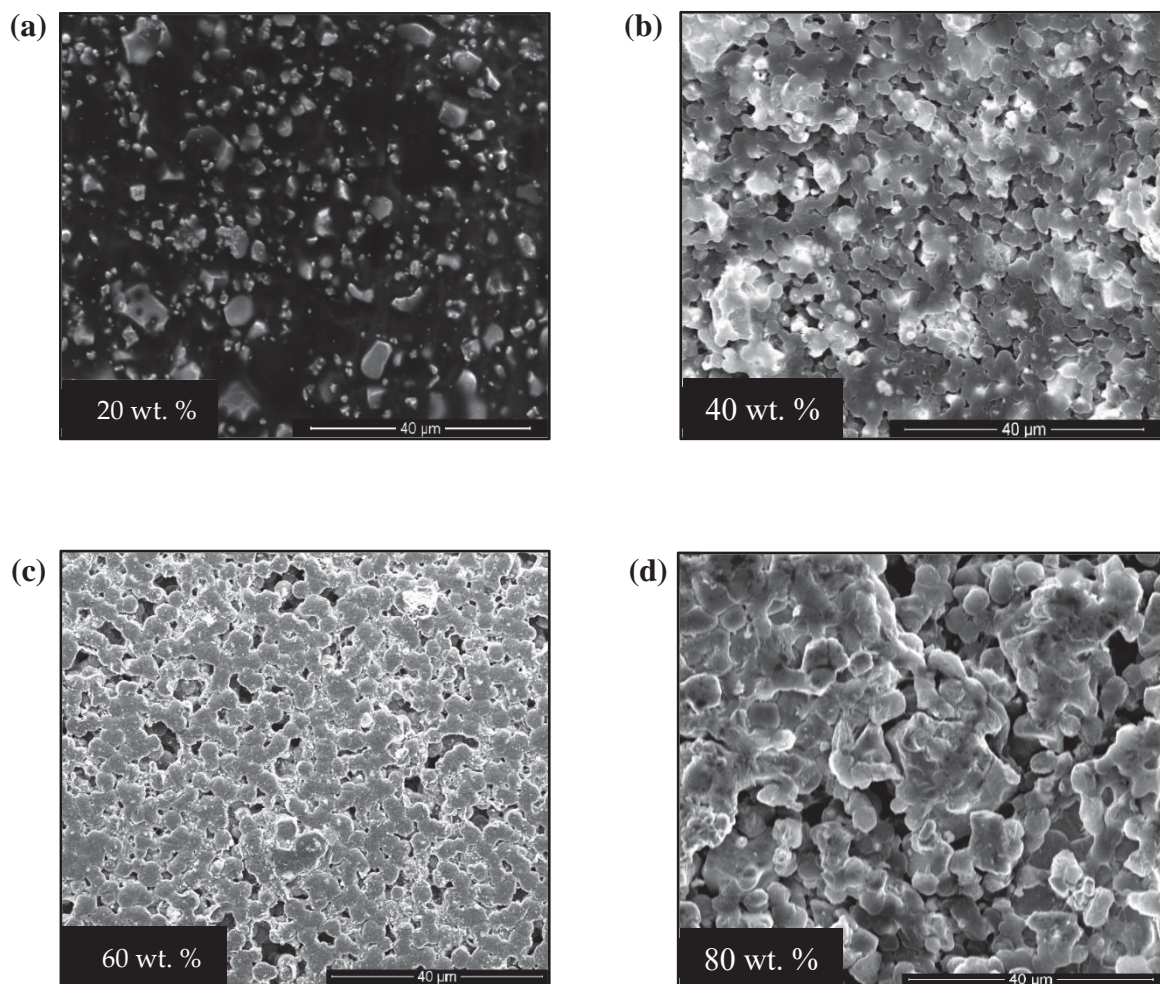
Figure 4.9 SEM images with different PVDF/PZT concentration (a) 20:80, (b) 40:60, (c) 60:40 and (d) 80:20.

Other fillers' micrographs, such as CCTO and CNT are also examined, as shown in Figure 4.10. CNTs are well adhered to the polymer matrix exhibiting flexibility, and stiffer than other samples. Favorable structural integrity is obtained from all the samples after hot pressing with the minimalized possibility of pores.
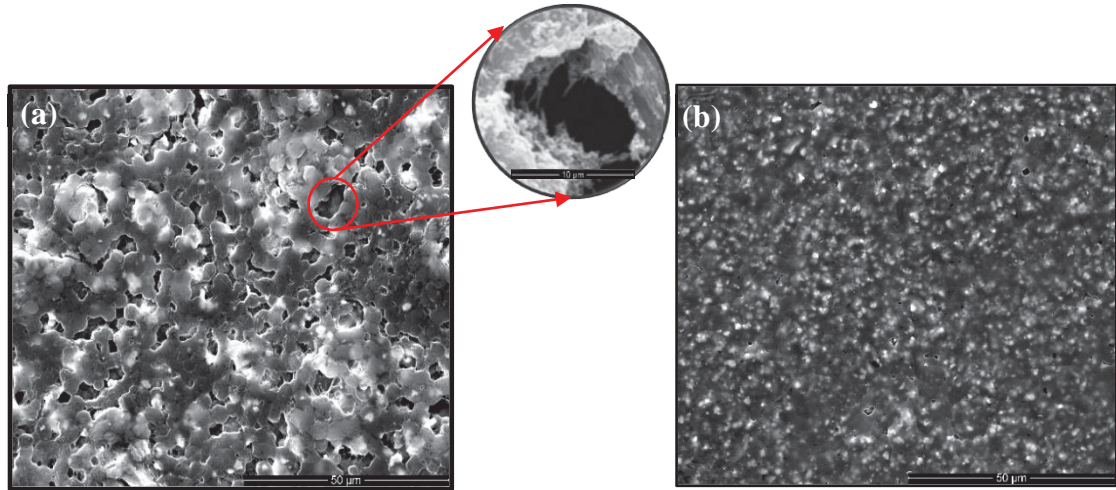
*Figure 4.10* SEM images (a) PVDF/PZT/CNTs (40:59.75:0.25), zoomed in picture shows CNTs and (b) PVDF/CCTO (40:60), showing a homogenous distribution of powder with less agglomeration.

4.3. Effect of Micro and Nano fillers in Dielectric Properties of PVDF polymer

From the major piezoelectric and dielectric properties mentioned in section 3.1, few vital properties such as piezoelectric stain coefficient (d_{33}), voltage (g_{33}) constant, and dielectric constant (ε_r) are analyzed for different composite types fabricated. The piezoelectric strain coefficient (d_{33}) is measured through electric charge generated in response to 0.25N force applied in thickness direction using a YE2730A piezometer, as shown in Figure 4.11. All the properties discussed in this section are measured and calculated using the previously defined methods and numbers are normalized in default given by the equipment utilized. The major factor to be noticed is the relation and trend among each properties which depends on the nature of filler added to the sample showcasing its distinct behavior.
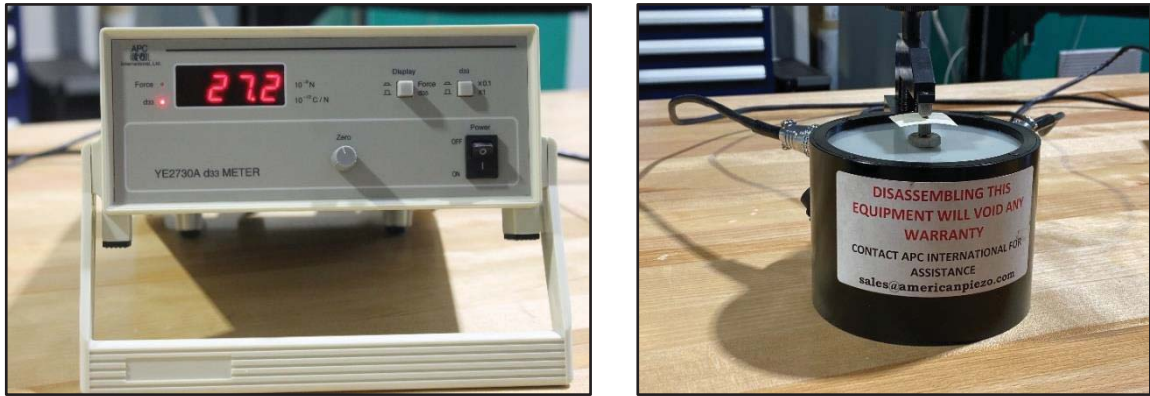
Figure 4.11 d_{33} measurement of fabricated piezoelectric samples.

Dielectric constant (ε_r), an essential property that enables the piezoelectric substrate to hold a charge for an extended period of time is calculated using the parallel plate capacitance standard relation. All the measured and calculated normalized properties are listed in Table 4.2.

Table 4.2

Measured piezoelectric and dielectric properties for different piezocomposite combinations.

Material	Thickness (mm)	d_{33} (pC/N)	ε_r	g_{33} (mVm/N)
PVDF	0.25	12.3	155.3	8.95
PVDF/PZT	0.51	21.6	247.5	9.86
PVDF/PZT/CNTs	0.82	17.4	948.9	2.07
PVDF/CNTs	0.72	33.5	725.2	5.22
PVDF/CCTO	0.60	12.5	388.2	3.64

From the measured properties, it can be noticed that when fillers are added to the

PVDF polymer dissolved in DMSO solvent, there is an overall increase in piezoelectric

property and the maximum piezoelectric strain coefficient (d_{33}) value is obtained in

PVDF with CNTs as filler. As the main goal of this research is to enhance the

piezoelectric properties, there is an evident increase in (d_{33}) after polarization, where the

effect of corona poling aligned the dipoles properly along the thickness direction with the

electric field applied. The enhanced strain coefficient before and after poling is

mentioned in Table 4.3.

Table 4.3

Effect of polarization in enhancing piezoelectric strain and voltage coefficient of the piezocomposites.

Material	Thickness (mm)	Polarized		% increase
		d_{33} (pC/N)	g_{33} (mVm/N)	
PVDF	0.25	16	11.64	30.08
PVDF/PZT	0.51	26	11.87	20.37
PVDF/PZT/CNTs	0.82	28	3.33	60.91
PVDF/CNTs	0.72	42	6.54	25.37
PVDF/CCTO	0.60	18	5.24	44

The dielectric constant (ε_r) is measured in different frequencies to evaluate the

frequency-dependent nature, which can be noticed in Figure 4.12. It can see that when the

frequency increases, the dielectric constant decreases because the net polarization drops

as the polarization mechanism gradually stop to contribute.
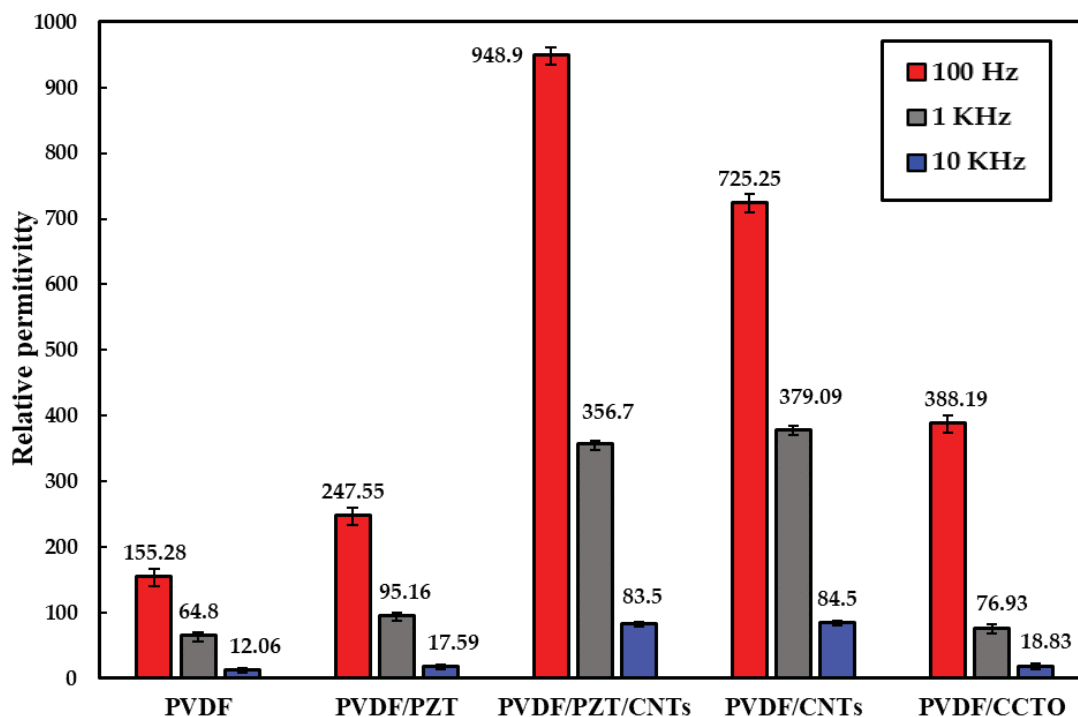
Figure 4.12 Frequency-dependent dielectric constant of PVDF mixed with different micro and nano fillers.

4.4. Effect of Micro and Nano fillers in PVDF Elastic Performance

To analyze the dynamic viscoelastic behavior and characterize material stiffness under temperature, DMA 8000 Perkin Elmer equipment is used at a constant frequency of 1Hz for different fabricated composite configuration. The temperature scan gives storage modulus, which is proportional to the stored energy (elastic response), and loss modulus, which is proportional to the energy dissipated (viscous response). Figure 4.13 describes the storage modulus (E') as a function of temperature at a constant frequency for all the different composites, which is measured using a tensile fixture.

It is observed that the storage modulus of PVDF is increased when micro and nano-fillers are incorporated, which can be attributed to their effectiveness in transferring the

interfacial stress and limiting the segmental motion of polymer chains. The measured

modulus values are listed in Table 4.4. The storage modulus at room temperature, also

termed as young's modulus, is a mechanical property that quantifies the relation between

stress and strain in the elastic region of the piezoelectric material. Table 4.4, displays the

young's modulus at room temperature for different samples.

Table 4.4

Young's modulus of PVDF with fillers.

Material	Young's modulus (GPa)
PVDF	1.64
PVDF/PZT	2.51
PVDF/PZT/CNTs	9.14
PVDF/CNTs	1.71
PVDF/CCTO	2.78

A maximum modulus of 9.14 GPa is obtained in sample with two combinations of

fillers such as PZT and CNTs, results in higher energy storage tendency when compared

with only PZT, CNT and CCTO fillers. It is evident that when the amount of fillers are

less, meaning only pure polymers, the tendency to restrict the molecular motion of PVDF

polymer is limited where less force is required for deformation, resulting in diminished

overall E' of the material with an increase in temperature. Additionally, the glass

transition temperature of PVDF is known to be in the negative temperature region, which

was not detected in the selected temperature range.
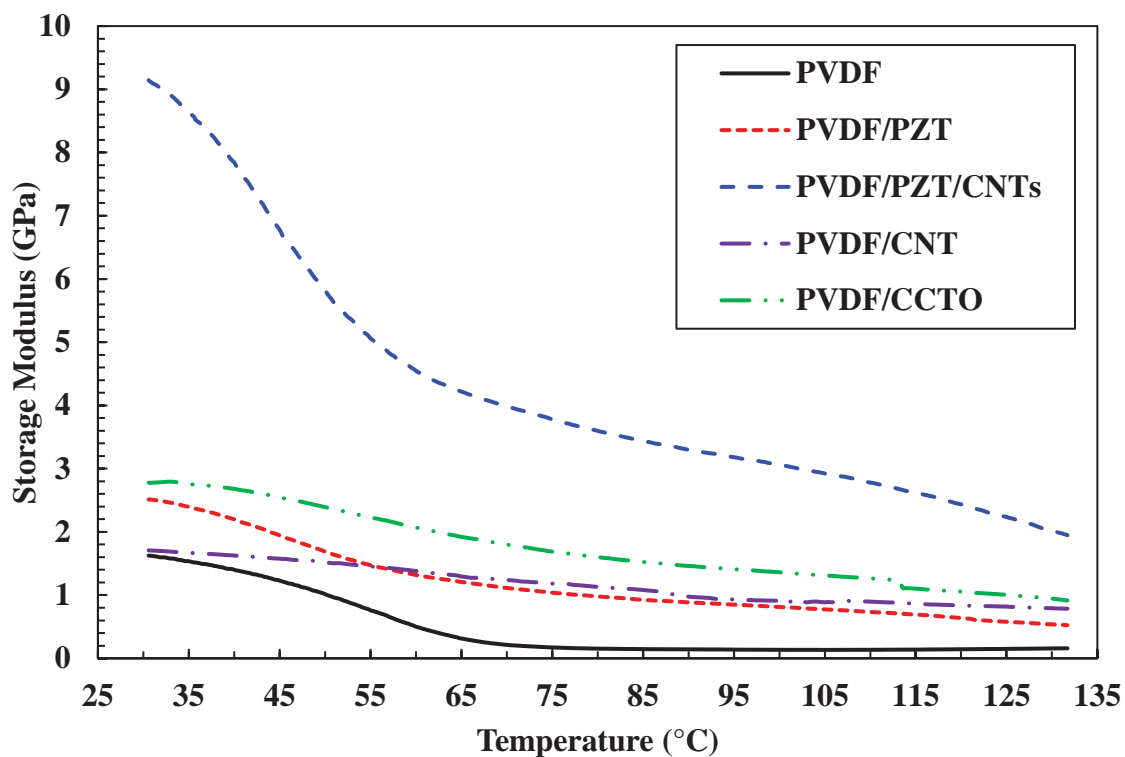
Figure 4.13 Storage modulus temperature sweep of PVDF polymer with different micro and nano fillers.

4.5. SAW Sensor Response using RF Testing

In this section, the fabricated substrate along with IDTs through selected fabrication technique is tested under condition applying RF signal by using electrical equipment. The response exported from the VNA, which contains useful information about the mechanical strains occurred in the host structure are analyzed deeper on how they relate to the overall objective of this research.

4.5.1 VNA Response

To determine the strain measuring capability of fabricated SAW sensor, VNA, a centralized DAQ system is used that validates the change in wave characteristics such as frequency and phase shifts. A network analyzer can generate input signal and analyze the

collected data from output signal like a full-duplex system. All scattering parameter data

model a device on how power flows into and out of the device terminals in a defined

transmission line, meaning this describes the input-output relationship between the ports.

The electro-acoustic behavior of the SAW sensor is investigated on its RF scattering

parameter response by connecting the network analyzer probes to the IDT terminals. An

RF signal is provided to the input IDT operated in the frequency range from 10 kHz –

100 MHz with a reference impedance of 50Ω. The fabricated SAW sensor is mounted on

a 7.62 cm x 7.62 cm steel plate with different angles (0°, 20°, and 40°), as shown in

Figure 4.14 (a).
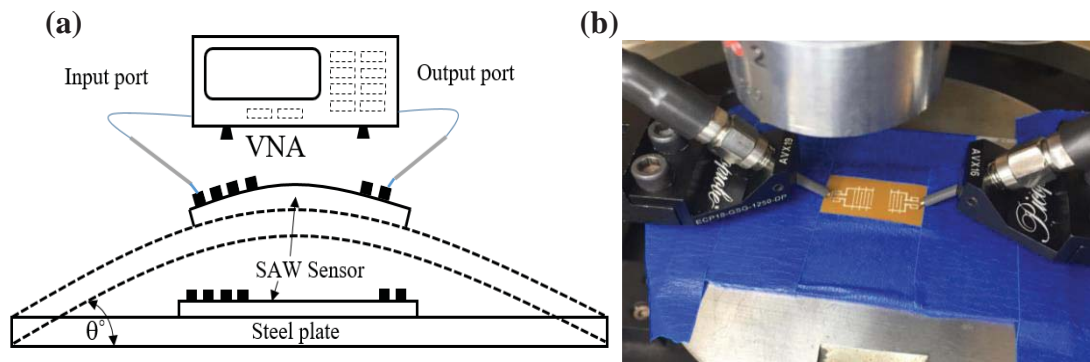
Figure 4.14 RF testing (a) VNA test setup with SAW sensor attached to a steel plate bent with angle θ; (b) probe setup connected to the SAW sensor terminal.

RF probing is performed on the sensor, as shown in Figure 4.14 (b) under different

bending conditions using a Keysight E5071C vector network analyzer, a probe station,

and two (ECP 18-GSG-1250-DP) GGB probes. The probes are calibrated using a CS-10

calibration substrate before every measurement cycle, where the insertion loss of the

sensor as a function of frequency is obtained. Figure 4.15 shows the probe station and

VNA used for frequency measurements. The frequency response mainly depends on the IDT's geometry and the velocity of the acoustic and electromagnetic waves propagated, which are related to the electromagnetic and acoustic properties of the substrate material. This scattering parameter can also be used in determining reflection coefficients in both single and two port SAW device. S_{21} represents the forward voltage gain response in the output IDT with the amount of power transmitted plotted with a function of frequency.

(a)

(b)
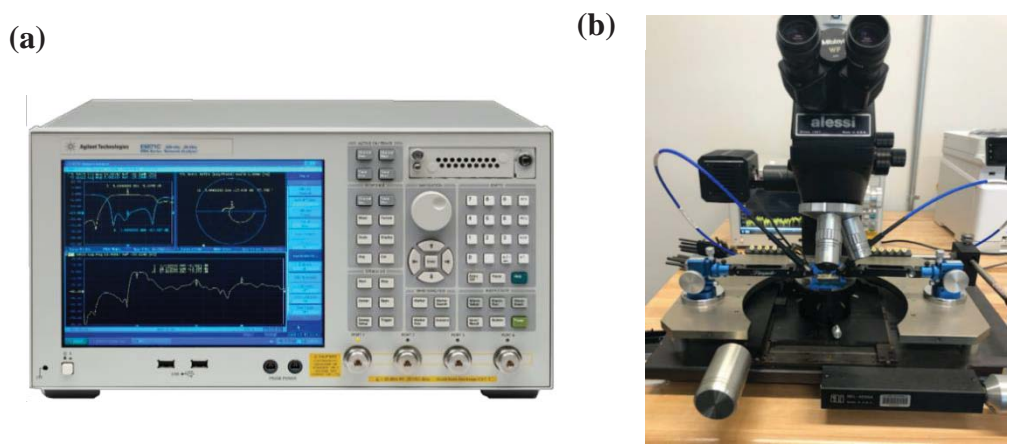
Figure 4.15 Electrical equipment (a) VNA used for RF testing; (b) Probe station for S_{21} measurement.
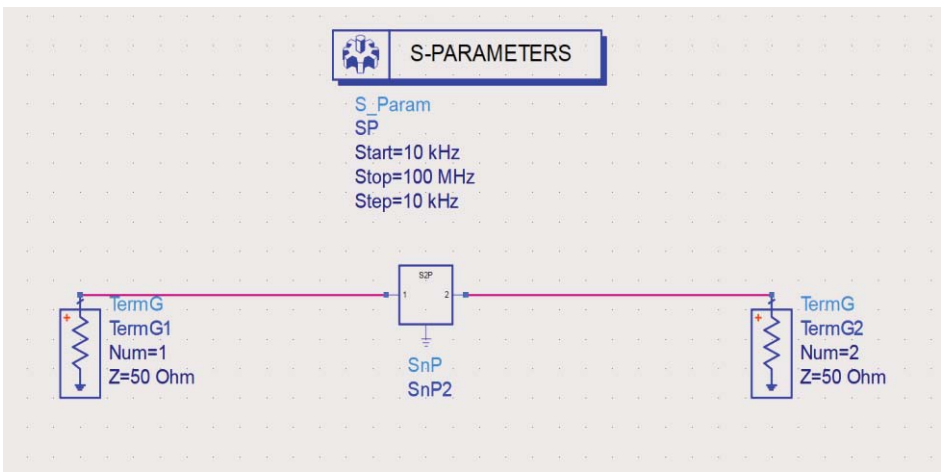

Figure 4.16 S-parameter circuit diagram in ADS software.

When the SAW sensor is bent, due to the deformation of the host structure, the composite substrate stretches, extending the delay line distance and finger spacing, which can be proportional to the shift in frequency response. The measured S-parameter is exported as .snp files that are used for post processing techniques. ADS software is used for simulating the extracted VNA data under different strain conditions. Figure 4.16 shows the circuit diagram that mimics the working of VNA for frequency response measurement in the ADS tool. Instead of being represented in decibel, S-parameter is transformed to phase angle in degree in which it is noticed that the frequency sweep is in phase influenced by perturbation with better transmission characteristics and fewer ripple disturbances.
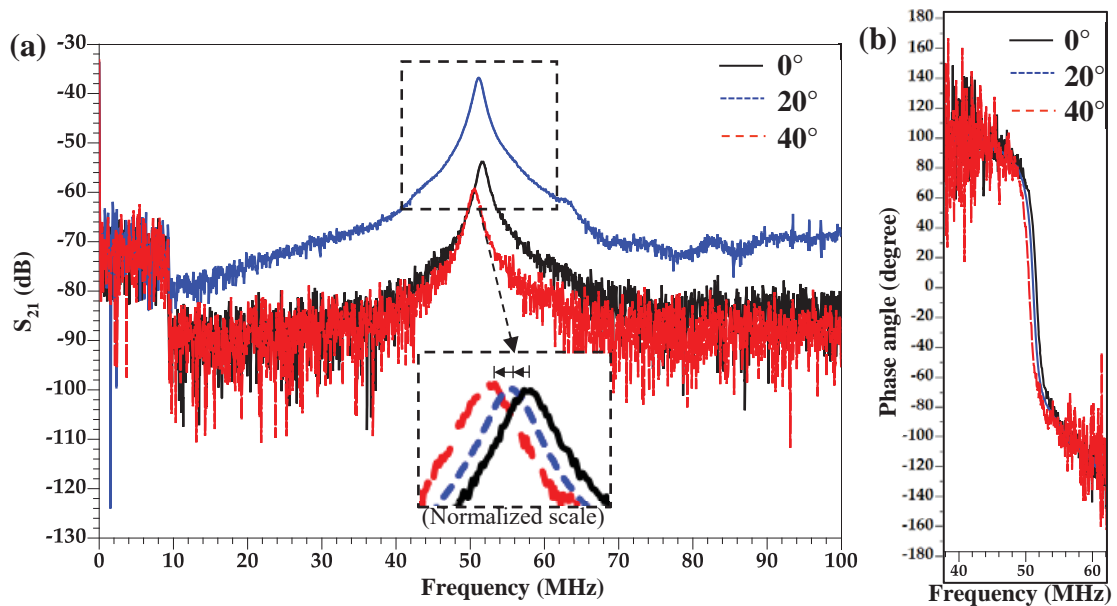

Figure 4.17 Frequency shift response of PVDF/PZT type (a) Frequency plot; (b) Phase plot; zoomed in box shows the peak shift in normalized frequency response when the SAW sensor is under bending in different angles.
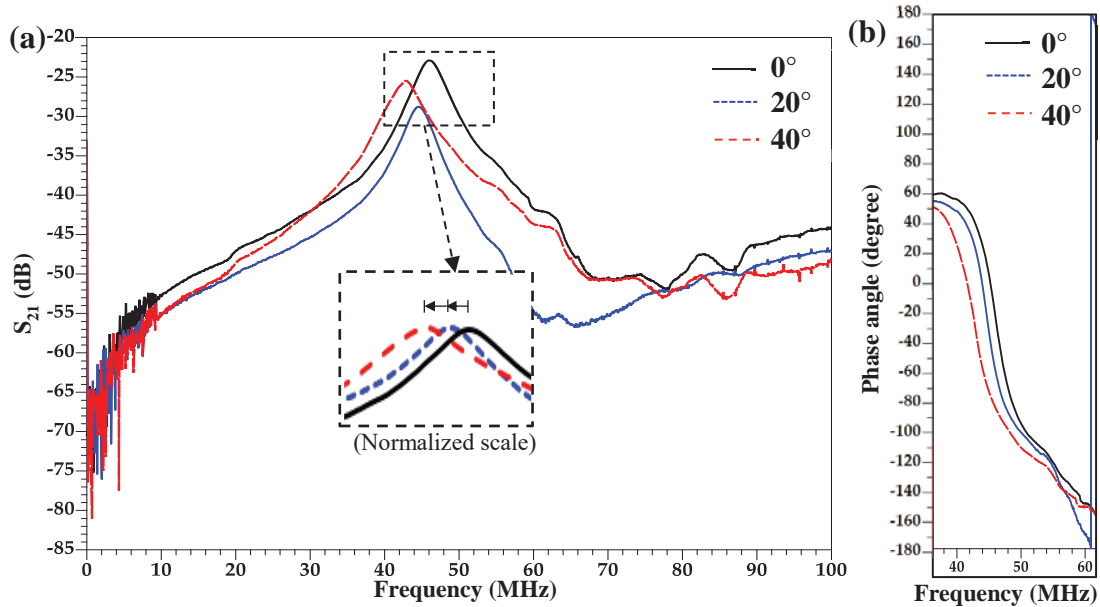
Figure 4.18 Frequency shift response of PVDF/PZT/CNTs type (a) Frequency; (b) Phase plot.

From the response of different fabricated SAW sensor, as shown from Figure 4.17 to 4.20, it is evident that each sensor type has its own resonance peak frequency corresponding to the wave characteristics of the substrate material. Each SAW sensor has fundamental and harmonic frequencies that are in phase and can be tuned to high frequency, which expands the range of applications.

The predominant peak is detected with the lower frequency range, but the fundamental frequency is not detected, which could be due to the impedance mismatch at 2.3 MHz, and the next close harmonic mode peak is tracked. Even with the lower frequency range, this VNA gives us almost noise under 10 MHz, which can be optimized further.
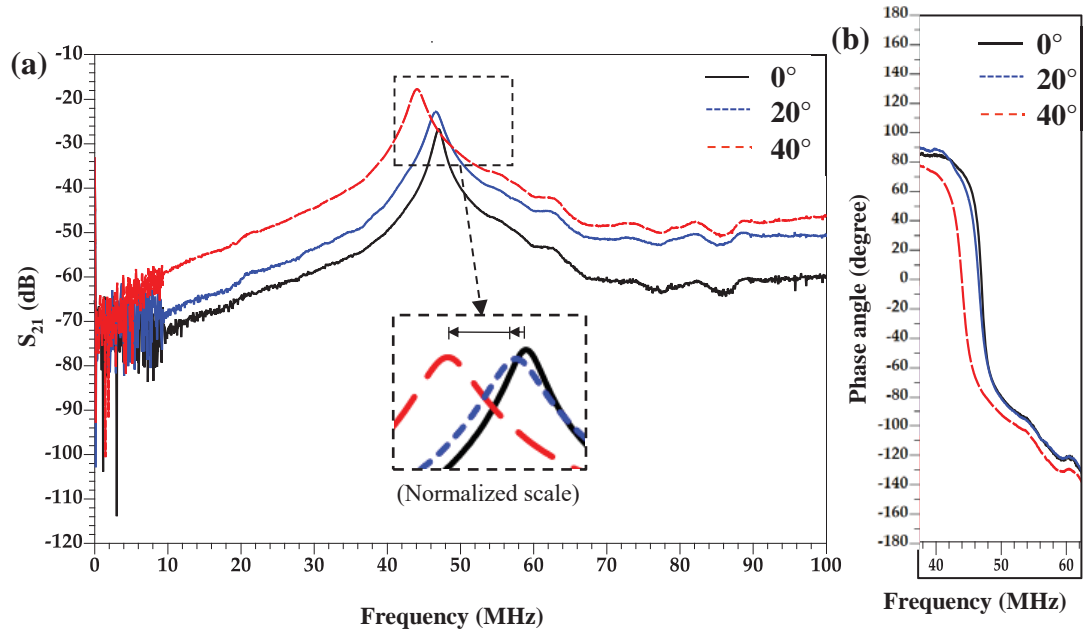
Figure 4.19 Response of PVDF/CNTs type (a) Frequency; (b) Phase plot.
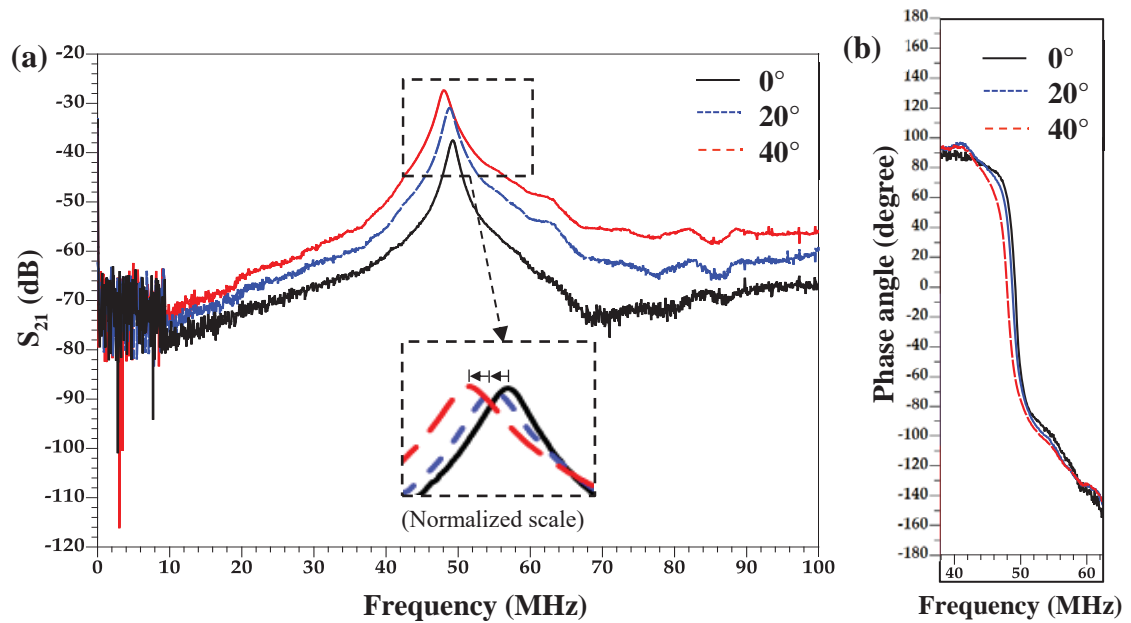

Figure 4.20 Response of PVDF/CCTO type (a) Frequency; (b) Phase plot.

A peak in S_{21} response is tracked between the different bending angles with an increase in strain, and Table 4.5 summarizes the frequency shift information of the peak

for all the samples. Insertion loss obtained in the frequency peaks can be reduced by optimal impedance matching and different IDT types to reduce reflections.

Table 4.5

Frequency shift data for different type of fillers in PVDF matrix.

Material	0° (MHz)	20° (MHz)	40° (MHz)
PVDF/PZT	51.57	51.13	50.57
PVDF/PZT/CNTs	45.95	44.57	42.88
PVDF/CNTs	47.01	46.63	44.07
PVDF/CCTO	49.26	48.82	48.01

4.6. Strain Quantification using DIC

In this section, the correlation host structure sprayed with speckle patterns are tracked by the commercially available Digital image correlation (DIC) optical technique, in order to determine the displacement occurred that can be correlated with the frequency response attained from the previous RF testing results.

4.6.1. Vic-3D Software for Quantitative Strain Post Processing

DIC system with two 6MP high resolution cameras are used to in which they are calibrated by using the calibration images to identify their location and angle between them focusing the host structure with SAW sensor mounted, as shown in Figure 4.21. The selected host structure (steel plate) is sprayed with a speckle pattern. Area under the sensor is the region of interest, which is selected in the VIC-3D software, as shown in Figure 4.22 and due to increase in applied strain, the camera will follow the speckle pattern of subsets to track the displacement in Y direction between consecutive images.

Figure 4.21 DIC technique measuring strain.
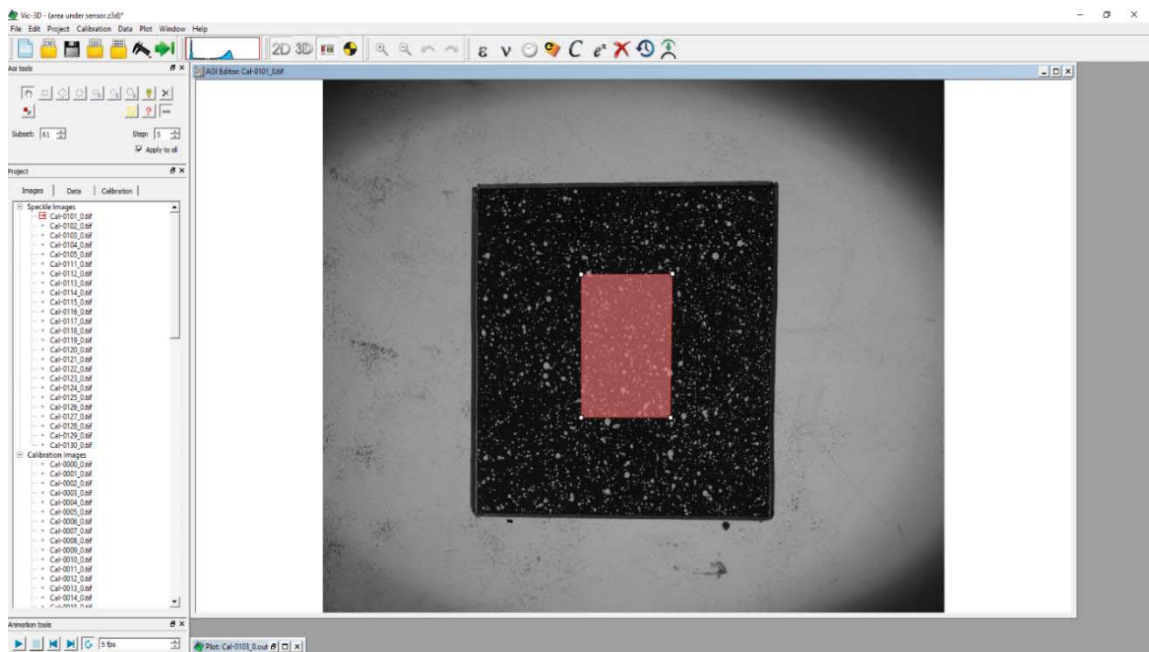
Figure 4.22 Range of interest area under SAW sensor to be analyzed in a selected host structure.

By using the non-contact optical technique, the quantitative strain is measured in three different angles using a correlation algorithm with a selected sensor area, as shown in Figure 4.23.
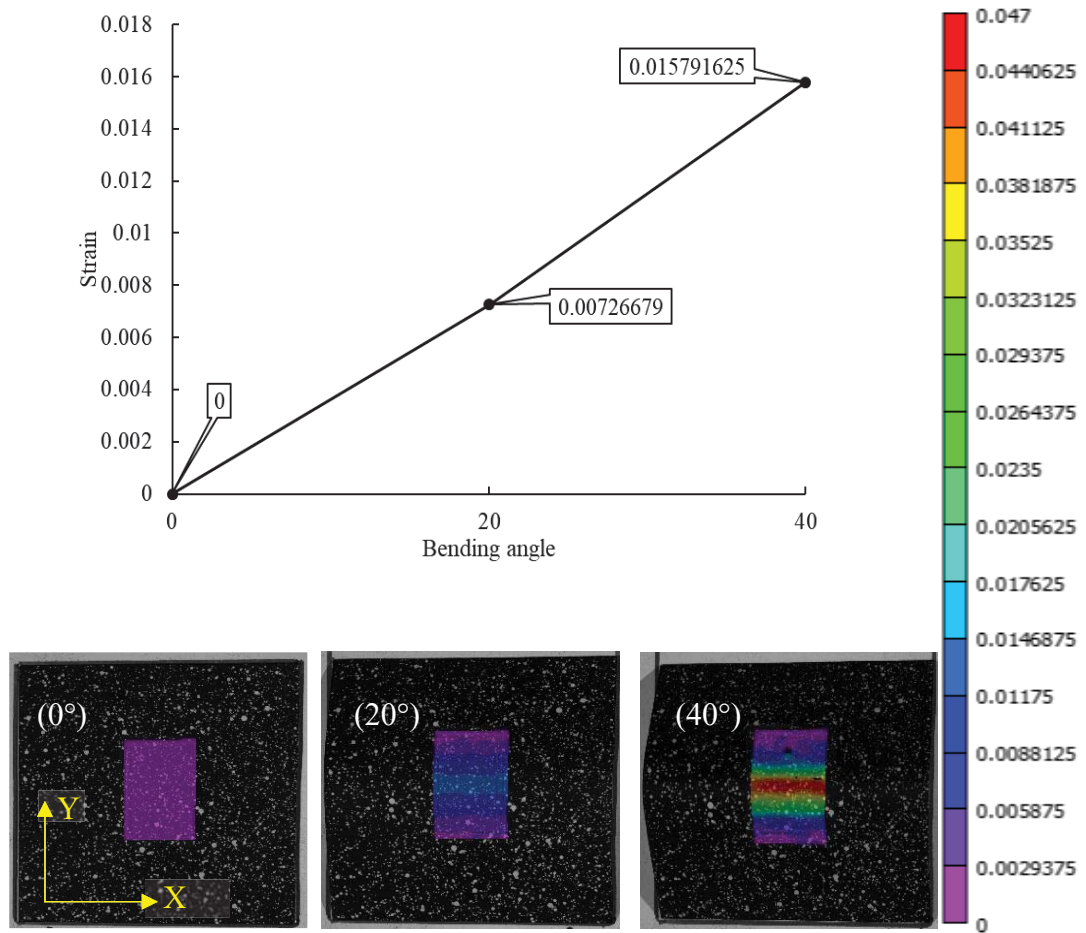

Figure 4.23 DIC measurement for different bending angles with correlation of displacement in Y direction; contour ranges pink as low to red as high strains.

5. Conclusion

The main objective and focus of this research was to develop a SAW sensor capable of detecting and measuring mechanical strain occurred in aerospace structures. It is observed that the fabricated substrate successfully detect mechanical strain and the substrate exhibiting higher piezoelectric properties along with flexibility. Summary collected throughout the research with recommendations and future works will be presented below.

5.1. Summary

In this research the fabrication and design of a piezoelectric composite sensor exhibiting flexibility made of PVDF as polymer matrix and different micro- and nano-fillers such as PZT, CCTO, and CNTs by a hot-press process is demonstrated. The different composites structural, morphological, thermal, and electrical properties are investigated through Fourier-transform infrared spectroscopy (FTIR), scanning electron microscope (SEM), differential scanning calorimetry (DSC), and dynamic mechanical analysis (DMA).

The printing of optimized IDTs design using the transmission matrix approach through direct digital manufacturing technique is described. Adding fillers to the polymer had a great impact on the piezoelectric property, especially the polar β phase and structural properties of the piezocomposite. For the composite, polar phase is enhanced by both stretching the piezoelectric material through hot-press and applying higher electric voltage, which the corona poling will reorient the dipole direction. The piezoelectric strain coefficient, voltage constant, and dielectric constant values are

enhanced significantly when the PVDF polymer is incorporated with both PZT (micro) and CNT nano-fillers while comparing with the counterparts.

PVDF/CNTs composite yields a maximum β phase fraction of 76.9 % as well as the maximum piezoelectric strain coefficient (d_{33}) of 42 pC/N. Other composite types also yield maximum property values, i.e., 948.9 dielectric constant (ε_r) by PVDF/PZT/CNTs and 11.87 mVm/N piezoelectric voltage constant with PVDF/PZT. Mechanical strains are detected and measured by utilizing the change in wave characteristics such as frequency shifts in the fabricated SAW sensor response. Results show a correlation between the measured frequency response and the quantitatively measured mechanical strains up to 15,800 µε at 40° bending angle, which is relatively high for this specific application.

5.2. Future Work

This research presented, mainly focuses on the fabrication of a flexible SAW sensor that can measure strain. With the fabricated sensor that can detect mechanical strains, there are some imminent works to be addressed. The frequency response obtained in the transmission model is with assumed wave velocity from the previous works. The velocity of the fabricated sample has to be measured using appropriate equipment in order to get the exact center frequency response. From the RF testing with the assumed velocity, it is uncertain that whether the wave generated is due to electromagnetic coupling or purely an acoustic coupling between the IDT and the piezoelectric substrate, which needs to be identified and is under analysis.

Further optimization of IDT design with less insertion loss should be designed and compared with ANSYS HFSS simulation responses. With the wired setup, there are few

limitations, such as real time measurement in the aircraft structure and embedding multiple sensors in a structure. By knowing the wireless capability, an antenna needs to be designed with the intended frequency range, which enables to measure strain with multiple sensors that could increase the measuring range area.

5.3. Recommendations

Due to the complex probing station, the plate bending technique is followed for strain measurement. By changing the probe setup, the sensor can be mounted in the cantilever beam and compared with another commercial product like strain gages. With the traditional techniques hot-press used in this research, there is always a separate technique is required after the substrate fabrication, especially for IDT deposition. This can be overcome by using additive manufacturing to the production of SAW device. Using a small diameter nozzle will allow increasing the number of fingers and reduce the spacing between them, which will results in increasing the fundamental frequency.

To achieve a higher precision frequency response, IDT design can be optimized using commercial FEA analysis tool such as COMSOL, ANSYS for a better understanding of the frequency response before fabrication. Insertion loss obtained with the present design is a little high and can be reduced by optimal impedance matching and different IDT types to reduce reflections. In this work, the fundamental frequency is not detected using the VNA, and we track the frequency peak of harmonic modes. Instead, the admittance can be measured in the required frequency range by using the BVD model. By tracking the shift in impedance plot, it will contain useful information about strain measurement. Material wise, PVDF-TrFE, a co-polymer of PVDF, looks promising in achieving higher piezoelectric strain and dielectric constant with a higher polar phase, and this avoids the

necessity of stretching. Fabrication using additive manufacturing can be studied in detail

and implemented to elude the limitations of used technique in this research.

REFERENCES

Araújo, E., & Eiras, J. (1999). Structural, electric and ferroelectric properties of PZT films obtained using oxide precursors. *Journal of Physics: Condensed Matter, 11*(8), 1975.

Arlt, K., & Wegener, M. (2010). Piezoelectric PZT/PVDF-copolymer 0-3 composites: aspects on film preparation and electrical poling. *IEEE Transactions on Dielectrics and Electrical Insulation, 17*(4), 1178-1184.

Aubert, T., Elmazria, O., & Assouar, M. (2009). *Wireless and batteryless surface acoustic wave sensors for high temperature environments.* Paper presented at the 2009 9th International Conference on Electronic Measurement & Instruments.

Ballato, A. (1995). Piezoelectricity: old effect, new thrusts. *IEEE transactions on ultrasonics, ferroelectrics, and frequency control, 42*(5), 916-926.

Benz, M., & Euler, W. B. (2003). Determination of the crystalline phases of poly (vinylidene fluoride) under different preparation conditions using differential scanning calorimetry and infrared spectroscopy. *Journal of applied polymer science, 89*(4), 1093-1100.

Brocato, R. W. (2004). Passive microwave tags. *Sandia National Laboratories*.

Cai, X., Lei, T., Sun, D., & Lin, L. (2017). A critical analysis of the α, β and γ phases in poly (vinylidene fluoride) using FTIR. *RSC advances, 7*(25), 15382-15389.

Cheeke, J. D. N. (2017). *Fundamentals and applications of ultrasonic waves*: CRC press.

Chen, D., Heyer, S., Ibbotson, S., Salonitis, K., Steingrímsson, J. G., & Thiede, S. (2015). Direct digital manufacturing: definition, evolution, and sustainability implications. *Journal of Cleaner Production, 107*, 615-625.

d'AMICO, A., Palma, A., & Verona, E. (1982). Palladium-surface acoustic wave interaction for hydrogen detection. *Applied Physics Letters, 41*(3), 300-301.

Defaÿ, E. (2013). *Integration of ferroelectric and piezoelectric thin films: concepts and applications for microsystems*: John Wiley & Sons.

Della Lucia, F., Zambrozi Jr, P., Frazatto, F., Piazzetta, M., & Gobbi, A. (2014). Design, fabrication and characterization of saw pressure sensors for extreme operation conditions. *Procedia Engineering, 87*, 540-543.

Devkota, J., Ohodnicki, P. R., & Greve, D. W. (2017). SAW sensors for chemical vapors and gases. *Sensors, 17*(4), 801.

Eun, K., Lee, K. J., Lee, K. K., Yang, S. S., & Choa, S.-H. (2016). Highly sensitive surface acoustic wave strain sensor for the measurement of tire deformation. *International Journal of Precision Engineering and Manufacturing, 17*(6), 699-707.

Fan, Y., Kong, P., Qi, H., Liu, H., & Ji, X. (2018). A surface acoustic wave response detection method for passive wireless torque sensor. *AIP Advances, 8*(1), 015321.

Ferreira, A., Martínez, M., Ansón-Casaos, A., Gómez-Pineda, L., Vaz, F., & Lanceros-Mendez, S. (2013). Relationship between electromechanical response and percolation threshold in carbon nanotube/poly (vinylidene fluoride) composites. *Carbon, 61*, 568-576.

Fraga, M. A., Furlan, H., Pessoa, R., & Massi, M. (2014). Wide bandgap semiconductor thin films for piezoelectric and piezoresistive MEMS sensors applied at high temperatures: an overview. *Microsystem technologies, 20*(1), 9-21.

Fu, C., Lee, K. J., Eun, K., Choa, S.-H., Lee, K., & Yang, S. S. (2016). Performance comparison of Rayleigh and STW modes on quartz crystal for strain sensor application. *Journal of Applied Physics, 120*(2), 024501.

Gao, L., Huang, Y., Hu, Y., & Du, H. (2007). Dielectric and ferroelectric properties of (1− x) BaTiO3–xBi0. 5Na0. 5TiO3 ceramics. *Ceramics International, 33*(6), 1041-1046.

García-Zaldívar, O., Escamilla-Díaz, T., Ramírez-Cardona, M., Hernández-Landaverde, M., Ramírez-Bon, R., Yañez-Limón, J., & Calderón-Piñar, F. (2017). Ferroelectric-paraelectric transition in a membrane with quenched-induced δ-phase of PVDF. *Scientific Reports, 7*(1), 1-8.

Ghosh, A., Zhang, C., Shi, S., & Zhang, H. (2019). High temperature CO2 sensing and its cross-sensitivity towards H2 and CO gas using calcium doped ZnO thin film coated langasite SAW sensor. *Sensors and Actuators B: Chemical, 301*, 126958.

Gonçalves, R., Lopes, A., Botelho, G., Neves, I. C., & Lanceros-Mendez, S. (2013). Influence of solvent properties on the electrical response of poly (vinylidene fluoride)/NaY composites. *Journal of Polymer Research, 20*(5), 143.

Gregorio Jr, R. (2006). Determination of the α, β, and γ crystalline phases of poly (vinylidene fluoride) films prepared at different conditions. *Journal of applied polymer science, 100*(4), 3272-3279.

Greve, D. W., Chin, T.-L., Zheng, P., Ohodnicki, P., Baltrus, J., & Oppenheim, I. J. (2013). Surface acoustic wave devices for harsh environment wireless sensing. *Sensors, 13*(6), 6910-6935.

Hempel, J., Finke, D., Steiert, M., Zeiser, R., Berndt, M., Wilde, J., & Reindl, L. (2013). *SAW strain sensors-high precision strain sensitivity investigation on chip-level.* Paper presented at the 2013 IEEE International Ultrasonics Symposium (IUS).

Holterman, J., & Groen, P. (2013). *An Introduction to piezoelectric materials and applications*: Stichting Applied Piezo.

Hu, B., Zhang, S., Zhang, H., Lv, W., Zhang, C., Lv, X., & San, H. (2019). Fabrications of L-Band LiNbO3-Based SAW Resonators for Aerospace Applications. *Micromachines, 10*(6), 349.

Jain, A., KJ, P., Sharma, A. K., Jain, A., & PN, R. (2015). Dielectric and piezoelectric properties of PVDF/PZT composites: a review. *Polymer Engineering & Science, 55*(7), 1589-1616.

Kang, H. M., Baek, S.-H., Song, J. H., Cho, Y. S., & Choi, J.-W. (2014). Full range dielectric characteristics of calcium copper titanate thin films prepared by continuous composition-spread sputtering. *ACS Combinatorial Science, 16*(9), 478-484.

Kawrani, S., Boulos, M., Cornu, D., & Bechelany, M. (2019). From synthesis to applications: copper calcium titanate (CCTO) and its magnetic and photocatalytic properties. *ChemistryOpen, 8*(7), 922-950.

Kharlamova, M. V., Kramberger, C., Domanov, O., Mittelberger, A., Yanagi, K., Pichler, T., & Eder, D. (2018). Fermi level engineering of metallicity-sorted metallic single-walled carbon nanotubes by encapsulation of few-atom-thick crystals of silver chloride. *Journal of Materials Science, 53*(18), 13018-13029.

Kim, H., Torres, F., Wu, Y., Villagran, D., Lin, Y., & Tseng, T.-L. B. (2017). Integrated 3D printing and corona poling process of PVDF piezoelectric films for pressure sensor application. *Smart Materials and Structures, 26*(8), 085027.

Kirbus, B., Brachmann, E., Hengst, C., & Menzel, S. (2018). Additive manufacturing of 96 MHz surface acoustic wave devices by means of superfine inkjet printing. *Smart Materials and Structures, 27*(7), 075042.

Korsah, K., Ma, C., & Dress, B. (1998). Harmonic frequency analysis of SAW resonator chemical sensors: application to the detection of carbon dioxide and humidity. *Sensors and Actuators B: Chemical, 50*(2), 110-116.

Kumar, G. S., Vishnupriya, D., Chary, K. S., & Patro, T. U. (2016). High dielectric permittivity and improved mechanical and thermal properties of poly (vinylidene fluoride) composites with low carbon nanotube content: effect of composite processing on phase behavior and dielectric properties. *Nanotechnology, 27*(38), 385702.

Li, F., Xiang, D., Chiang, S., Tittmann, B. R., & Searfass, C. (2011). *Wireless surface acoustic wave radio frequency identification (SAW-RFID) sensor system for temperature and strain measurements.* Paper presented at the 2011 IEEE International Ultrasonics Symposium.

Li, Q., Liu, J., Yang, B., Lu, L., Yi, Z., Tian, Y., & Liu, J. (2019). Highly sensitive surface acoustic wave flexible strain sensor. *IEEE Electron Device Letters, 40*(6), 961-964.

Li, S., Sankaranarayanan, S. K., Fan, C., Su, Y., & Bhethanabotla, V. R. (2017). Achieving lower insertion loss and higher sensitivity in a SAW biosensor via optimization of waveguide and microcavity structures. *IEEE Sensors Journal, 17*(6), 1608-1616.

Liu, L., & Grunlan, J. C. (2007). Clay assisted dispersion of carbon nanotubes in conductive epoxy nanocomposites. *Advanced Functional Materials, 17*(14), 2343-2348.

Mahadeva, S. K., Berring, J., Walus, K., & Stoeber, B. (2013). Effect of poling time and grid voltage on phase transition and piezoelectricity of poly (vinyledene fluoride) thin films using corona poling. *Journal of Physics D: Applied Physics, 46*(28), 285305.

McGrath, M. J., Ni Scanaill, C., & Nafus, D. (2013). *Sensor technologies: healthcare, wellness, and environmental applications*: Springer Nature.

Medeiros, K. A. R., Rangel, E. Q., Sant'Anna, A. R., Louzada, D. R., Barbosa, C. R. H., & d'Almeida, J. R. M. (2018). Evaluation of the electromechanical behavior of polyvinylidene fluoride used as a component of risers in the offshore oil industry. *Oil & Gas Science and Technology–Revue d'IFP Energies nouvelles, 73*, 48.

Miyata, Y., Mizuno, K., & Kataura, H. (2011). Purity and defect characterization of single-wall carbon nanotubes using Raman spectroscopy. *Journal of Nanomaterials, 2011*.

Mould, R. F. (2007). Pierre Curie, 1859–1906. *Current oncology, 14*(2), 74.

Mujahid, A., & Dickert, F. L. (2017). Surface acoustic wave (SAW) for chemical sensing applications of recognition layers. *Sensors, 17*(12), 2716.

Newnham, R., Skinner, D., & Cross, L. (1978). Connectivity and piezoelectric-pyroelectric composites. *Materials Research Bulletin, 13*(5), 525-536.

Ngo, T. D., Kashani, A., Imbalzano, G., Nguyen, K. T., & Hui, D. (2018). Additive manufacturing (3D printing): A review of materials, methods, applications and challenges. *Composites Part B: Engineering, 143*, 172-196.

Nicolay, P., Chambon, H., Bruckner, G., Gruber, C., Ballandras, S., Courjon, E., & Stadler, M. (2018). A LN/Si-Based SAW Pressure Sensor. *Sensors, 18*(10), 3482.

Nomura, T., Kosaka, T., Saitoh, A., & Furukawa, S. (2006). Passive strain sensor using SH-SAW reflective delay line. *Ferroelectrics, 333*(1), 121-129.

Oh, H., Lee, K., Eun, K., Choa, S.-H., & Yang, S. S. (2012). Development of a high-sensitivity strain measurement system based on a SH SAW sensor. *Journal of Micromechanics and Microengineering, 22*(2), 025002.

Osse, J. (2017). Development of a flexible saw sensor for strain sensing.

Ouyang, X., Cao, P., Zhang, W., Liu, Z., Huang, Z., & Gao, W. (2015). CaCu 3 Ti 4 O 12–PVDF polymeric composites with enhanced capacitive energy density. *International Journal of Modern Physics B, 29*(10n11), 1540003.

Panda, P. (2017). Piezoceramic materials and devices for aerospace applications. In *Aerospace Materials and Material Technologies* (pp. 501-518): Springer.

Peng, Y., Sun, B., & Wu, P. (2008). Two-dimensional correlation infrared spectroscopic study on the crystallization and gelation of poly (vinylidene fluoride) in cyclohexanone. *Applied spectroscopy, 62*(3), 295-301.

Piezoelectricity, I. S. o. (1987). ANSI/IEEE Std 176–1987. In: American Standards National Institute New York, USA, NY.

Prabakaran, K., & Sujatha, L. Study of Surface Acoustic Wave Sensor.

Pramanik, S., Pingguan-Murphy, B., & Osman, N. A. (2013). Developments of immobilized surface modified piezoelectric crystal biosensors for advanced applications. *Int. J. Electrochem. Sci, 8*, 8863-8892.

Rayleigh, L. (1885). On wave propagated along the plane surface of an elastic solid. *Proceesings of the London mathematical Soceity,* 1(1)*,* 4-11.

Reindl, L., Scholl, G., Ostertag, T., Ruppel, C., Bulst, W.-E., & Seifert, F. (1996). *SAW devices as wireless passive sensors.* Paper presented at the 1996 IEEE Ultrasonics Symposium. Proceedings.

Rickert, J., Göpel, W., Hayward, G. L., Cavic, B. A., & Thompson, M. (1999). Biosensors based on acoustic wave devices. *Sensors Update, 5*(1), 105-139.

Ro, R., Tung, H.-Y., & Wu, S.-J. (2004). Design of two-track surface acoustic wave filters with width-controlled reflectors. *Japanese journal of applied physics, 43*(2R), 688.

Roy, R. E., Vijayalakshmi, K., Bhuvaneswari, S., & Rajeev, R. (2019). Influence of process conditions and effect of functionalization in inducing time dependent polymorphic states in single walled carbon nanotube incorporated poly (vinylidene fluoride). *SN Applied Sciences, 1*(9), 978.

Ruan, L., Yao, X., Chang, Y., Zhou, L., Qin, G., & Zhang, X. (2018). Properties and Applications of the β Phase Poly (vinylidene fluoride). *Polymers, 10*(3), 228.

Salimi, A., & Yousefi, A. (2003). Analysis method: FTIR studies of β-phase crystal formation in stretched PVDF films. *Polymer Testing, 22*(6), 699-704.

Salimi, A., & Yousefi, A. A. (2004). Conformational changes and phase transformation mechanisms in PVDF solution-cast films. *Journal of Polymer Science Part B: Polymer Physics, 42*(18), 3487-3495.

Sanati, M., Sandwell, A., Mostaghimi, H., & Park, S. S. (2018). Development of Nanocomposite-Based Strain Sensor with Piezoelectric and Piezoresistive Properties. *Sensors, 18*(11), 3789.

Seema, A., Dayas, K., & Varghese, J. M. (2007). PVDF-PZT-5H composites prepared by hot press and tape casting techniques. *Journal of applied polymer science, 106*(1), 146-151.

Shu, L., Peng, B., Yang, Z., Wang, R., Deng, S., & Liu, X. (2015). High-temperature SAW wireless strain sensor with langasite. *Sensors, 15*(11), 28531-28542.

Shu, L., Wang, X., Li, L., Yan, D., Peng, L., Fan, L., & Wu, W. (2019). The investigation of integrated SAW strain sensor based on AlN/TC4 structure. *Sensors and Actuators A: Physical, 293*, 14-20.

Stoney, R., Donohoe, B., Geraghty, D., & O'Donnell, G. (2012). The development of surface acoustic wave sensors (SAWs) for process monitoring. *Procedia Cirp, 1*, 569-574.

Stowell, W., & Weise, R. (1983). *Application of thin film strain gages and thermocouples for measurement on aircraft engine parts.* Paper presented at the 19th Joint Propulsion Conference.

Thiruramanathan, P., Marikani, A., Ravi, S., Madhavan, D., & Hikku, G. (2018). Fabrication of miniaturized high bandwidth dielectric resonator on patch (DRoP) antenna using high dielectric CaCu3Ti4O12 nanoparticles. *Journal of Alloys and Compounds, 747*, 1033-1042.

Thongsanitgarn, P., Watcharapasorn, A., & Jiansirisomboon, S. (2010). Electrical and mechanical properties of PZT/PVDF 0–3 composites. *Surface review and letters, 17*(01), 1-7.

Tsentalovich, D. E., Headrick, R. J., Mirri, F., Hao, J., Behabtu, N., Young, C. C., & Pasquali, M. (2017). Influence of carbon nanotube characteristics on macroscopic fiber properties. *ACS applied materials & interfaces, 9*(41), 36189-36198.

Udd, E., Schulz, W. L., Seim, J. M., Trego, A., Haugse, E. D., & Johnson, P. E. (2000). *Transversely loaded fiber optic grating strain sensors for aerospace applications.* Paper presented at the Nondestructive Evaluation of Aging Aircraft, Airports, and Aerospace Hardware IV.

Vicente, J., Costa, P., Lanceros-Mendez, S., Abete, J. M., & Iturrospe, A. (2019). Electromechanical properties of PVDF-based polymers reinforced with nanocarbonaceous fillers for pressure sensing applications. *Materials, 12*(21), 3545.

Waller, D., & Safari, A. (1988). Corona poling of PZT ceramics and flexible piezoelectric composites. *Ferroelectrics, 87*(1), 189-195.

Wang, H., Cai, H., Zhou, W., & Liu, S. (2019). Poly (Vinylidene Fluoride)/Mg Doped CaCu 3 Ti 4 O 12 Composites with Improved Dielectric Properties. *MS&E, 472*(1), 012008.

Wang, P., Pan, Z., Wang, M., Huang, S., Liu, J., & Zhai, J. (2019). Polypyrrole random-coil induced permittivity from negative to positive in all-organic composite films. *Journal of Materiomics*.

Wang, X., Sun, F., Yin, G., Wang, Y., Liu, B., & Dong, M. (2018). Tactile-sensing based on flexible PVDF nanofibers via electrospinning: A review. *Sensors, 18*(2), 330.

White, R. M., & Voltmer F. W. (1965). Direct piezoelectric coupling to surface elastic waves. *Applied Physics Letters, 7*(12), 314-316.

Yan, X., Suzuki, T., Kitahama, Y., Sato, H., Itoh, T., & Ozaki, Y. (2013). A study on the interaction of single-walled carbon nanotubes (SWCNTs) and polystyrene (PS) at the interface in SWCNT–PS nanocomposites using tip-enhanced Raman spectroscopy. *Physical Chemistry Chemical Physics, 15*(47), 20618-20624.

Yao, X., Luan, C., & Fu, J. (2016). Transmission and measurement characteristics evaluation of surface acoustic wave sensor on rotating spindle in machine tools. *Advances in Mechanical Engineering, 8*(11), 1687814016676782.

Zhang, J., Zheng, P., Shao, S., Su, W., & Wang, C. (2007). Dielectric and electrical properties of CaCu3Ti4O12 ceramics at high temperatures. *Ferroelectrics, 356*(1), 85-89.

Zheng, P., Zhang, R.-z., Chen, H.-y., & Hao, W.-t. (2014). Thermoelectric Properties and Conduction Mechanism of CaCu 3 Ti 4 O 12 Ceramics at High Temperatures. *Journal of electronic materials, 43*(6), 1645-1649.

APPENDIX

```
%Simulation of the frequency response of SAW delay line sensor %Rishi
clear all;
clc;
v=3000;                            %SAW velocity on the free sections
of PVDF_PZT composite
v_m=2800;                          %SAW velocity on the metallized
sections of PVDF_PZT composite
lambda_0=1.3e-3;                   %SAW wavelength
f0=v/lambda_0;                     %center frequency
Nf_in=6;                            %Number of electrodes in the input
IDT
Nf_out=4;                           %Number of electrodes in the
output IDT
BBH=0.25e-3;                        %Bus bar height
C_fp=500e-12;                       %Capacitance per finger pair per
unit length
k=sqrt(0.0014);                     %Electromechanical coupling
coefficient of PVDF_PZT composite
df=0.25/1.3*lambda_0;               %free section 1/3*lambda
dm=0.15/1.3*lambda_0;               %metallized section 1/6*lambda
fm=v_m/lambda_0;                    %frequency of metallized _section
W=4e-3;                            %Acoustic aperture , factor=80 to
d=3.75e-3;                         %Length of the delay
line(transmission line )
Z=1/(f0*C_fp*W*k;                  %acoustic impedance for free
sections without fingers
Z_m=1/(fm*C_fp*W*k);               %acoustic impedance for the
metallized sections with fingers
k11=(0.016+(0.02*BBH/lambda_0))*(2*pi/lambda_0); %Self coupling
coefficient of PVDF_PZT composite
i=1;
for f=1.2e6:100:3.4e6                      %Frequency range
    lambda=v/f;
    omega=2*pi*f;

    %Computation of the ABCD matrix for a single finger
    theta_f=2*pi*f*df /v;              %acoustic angle in free region
    theta_m=2*pi*f*dm/v_m;            %acoustic angle in metallized
region
    %Computation of the free region between fingers
    Af=cos(theta_f);
    Bf=sqrt(-1)*Z*sin(theta_f);
    Cf=sqrt(-1)*sin(theta_f)/Z;
    Df=cos(theta_f);
    %Computation of the metallized regions under fingers
    Am=cos(theta_m);
    Bm=sqrt(-1)*Z_m*sin (theta_m);
    Cm=sqrt(-1)*sin(theta_m)/Z_m;
    Dm=cos(theta_m);
    %Cascading matrix for a single finger to calculate 2x2 Afinger
matrix
    Afinger =[Af Bf;Cf Df]*[Am Bm;Cm Dm]*[Af Bf;Cf Df];
    %Single finger matrix value
```

```matlab
    A_se=Afinger (1,1);
    B_se=Afinger (1,2);
    C_se=Afinger (2,1);
    D_se=Afinger (2,2);
    theta_d=2*pi*f*d/v;              %delay path
    theta_e=acos(A_se);
    Ze=B_se/(sqrt(-1)*sin(theta_e));

    %2x2 transmission matrix for a single finger of the IDT
    t11 =0.5*(2*A_se+(B_se/Z)+Z*C_se);
    t12 =0.5*(Z*C_se-(B_se/Z));
    t13 =((sqrt (-1)*tan(theta_e/2)*(Z^0.5))/(2*Ze))*(-A_se-1-
(B_se/Z));
    t21=-t12;
    t22=conj(t11);
    t23=sqrt(-1)*tan(theta_e/2)*(Z^0.5)*(1+A_se-(B_se/Z))/(2*Ze);
    t31=2*t13;
    t32=-2*t23;
    t33=sqrt(-1)*omega*C_fp*W*0.5+ sqrt(-1)*2*(tan(theta_e/2)/Ze)-
sqrt(-1)*(sin(theta_e )*(tan(theta_e/2)^2))/Ze;

    %computing the 2x2 IDT matrix
    t1 =[t11 t12;t21 t22]^Nf_in;      %2x2 scattering matrix
T_p^N_input (N finger pairs )
    t3 =[t11 t12;t21 t22]^Nf_out;     %2x2 scattering matrix
T_p^N_output(N finger pairs )
    t111=t1(1,1);
    t121=t1(1,2);
    t211=t1(2,1);
    t221=t1(2,2);
    t123=t3(1,2);
    t113=t3(1,1);
    t213=t3(2,1);
    t223=t3(2,2);
    Bp=[t13;t23]+[t11 t12;t21 t22]*[-t13;-t23];
    Cp=[t31 t32]*[t11 t12;t21 t22]+[-t31 -t32];
    t33p=2*t33 +[t31 t32]*[-t13;-t23];
    Tp=[t11 t12;t21 t22]^2;
    B_Nin=[0;0];
    C_Nin=[0 0];
    B_Nout=[0;0];
    C_Nout=[0 0];
    t333=(Nf_out/2)*t33p ;            %Initial value for t333
    t331=(Nf_in/2)*t33p ;            %Initial value for t331

    %computing t13, t23, t31, t32, t33 values for the whole IDT
    %Input IDT
    for i1=1:(Nf_in/2)
        B_Nin=B_Nin+(Tp^(i1-1))*Bp;
        C_Nin=C_Nin+Cp*Tp^(i1-1);
        t331=t331+((Nf_in/2)-i1)*Cp*Tp^(i1-1)*Bp;
    end
    %Reflector&output IDT
    for i2=1:(Nf_out/2)
        B_Nout=B_Nout+(Tp^(i2-1))*Bp;
        C_Nout=C_Nout+Cp*Tp^(i2-1);
```

```
        t333=t333+((Nf_out/2)-i2)*Cp*Tp^(i2-1)*Bp;
    end

    t131=B_Nin(1,1);
    t133=B_Nout(1,1);
    t231=B_Nin(2,1);
    t233=B_Nout(2,1);
    t311=C_Nin(1,1);
    t313=C_Nout(1,1);
    t321=C_Nin(1,2);
    t323=C_Nout(1,2);
    %ABCD matrix of delay path
    Ad=cos(theta_d);
    Bd=sqrt(-1)*Z*sin (theta_d);
    Cd=sqrt(-1)*sin(theta_d)/Z;
    Dd=cos(theta_d);
    %Computation of transmission matrix for delay path
    d11=0.5*(2*Ad+(Bd/Z)+Z*Cd);
    d12=0.5*(Z*Cd-(Bd/Z));
    d21=-d12;
    d22=0.5*(2*Ad-(Bd/Z)-Z*Cd);
    d2=[d11 d12;d21 d22];

    %Used substitutions for convenience
    M=t1*d2*t3;
    K=t1*d2*[t133;t233];
    P=[t311 t321]*d2*t3;
    L=[t311 t321]*d2*[t133;t233];
    %computing Y parameter ( Admittance ) for the SAW delay line
    y11(i)=t331-(P(1,1)*t131/M(1,1));
    y12(i)=L(1,1)-(P(1,1)*K(1,1)/M(1,1));
    y21(i)=-t313*t131/M(1,1);
    y22(i)=t333-(t313*K(1,1)/M(1,1));
    %Computing frequency response S21 using the Y parameter
    s11(i)=((1-
y11(i))*(1+y22(i))+y12(i)*y21(i))/((1+y11(i))*(1+y22(i))-
y12(i)*y21(i));
    s12(i)=-2*y12(i)/((1+y11(i))*(1+y22(i))-y12(i)*y21(i));
    s21(i)=-2*y21(i)/((1+y11(i))*(1+y22(i))-y12(i)*y21(i));
    s22(i)=((1+y11(i))*(1-
y22(i))+y12(i)*y21(i))/((1+y11(i))*(1+y22(i))-y12(i)*y21(i));
    %Computing Z parameter as impedance
    z11=((1+s11(i))*(1-s22(i))+s12(i)*s21(i))/((1-s11(i))*(1-s22(i))-
s12(i)*s21(i));
    z12=2*s12(i)/((1-s11(i))*(1-s22(i))-s12(i)*s21(i));
    z21=2*s21(i)/((1-s11(i))*(1-s22(i))-s12(i)*s21(i));
    z22=((1-s11(i))*(1+ s22(i))+s12(i)*s21(i))/((1-s11(i))*(1-s22(i))-
s12(i)*s21(i));
    %modified S°parameter including source and load impedance
    s21_n(i)=-50*z12/(z12^2-(z11+50)*(z22+50));
    i=i+1;
end

figure(1);
f=1.2e6:100:3.4e6;
y1=20*log10(abs(s21_n));
```

```matlab
y2=angle(s21_n)*180/pi;
yyaxis left
plot(f,y1,'b')
% title('Frequency Response','FontSize',18);
xlabel('Frequency/Hz','fontweight','bold','FontSize',16);
ylabel('S21/dB','fontweight','bold','FontSize',16)
set(findall(gca,'type','line'),'linewidth',1)
% grid on
yyaxis right
plot(f,y2,'-.r')
ylabel('Phase angle/degrees','FontSize',14)
ylim([-200 200] )
```